Improving Galactic Center Astrometry by Reducing the Effects of Geometric Distortion

S. Yelda[1], J. R. Lu[2], A. M. Ghez[1,3], W. Clarkson[1], J. Anderson[4], T. Do[1], M. R. Morris[1], K. Matthews[2]

ABSTRACT

The recent advent of adaptive optics systems on 8-10 m class telescopes has allowed for sub-milliarcsecond astrometry from the ground on a wide variety of astronomical objects. However, while the relative astrometry of the Galactic center is currently limited to a mere $\sim$0.2 mas, the *absolute* astrometry in this region has been limited to $\sim$6 mas at Keck. In this paper, we identify and correct major limitations to our absolute astrometry - geometric optical distortion and differential atmospheric refraction. These effects introduce $\sim$1-5 mas scale distortions over the spatial scales of the SiO masers that are used to define the absolute reference frame for proper motions of stars at the GC. With new observations of M92 at a wide variety of positions and orientations, we improve upon existing geometric distortion solutions for the NIRC2 narrow camera at the W. M. Keck II 10 m telescope. Post-fit residuals are reduced by a factor of $\sim$2-4 over previous solutions. To illustrate the impact of the refinements made here, we show that an absolute astrometric reference frame for the Galactic center can now be established to within 0.3 mas/yr, which is a factor of $\gtrsim$3 improvement over earlier work. Furthermore, we report on updated properties of the central supermassive black hole based on the orbit of the central arcsecond star, S0-2. The gains in our astrometric accuracy will also improve our ability to measure relatively small stellar accelerations at large radii. This distortion solution is available to the public in the form of FITS files.

---

[1]UCLA Department of Physics and Astronomy, Los Angeles, CA 90095 -1547; syelda, ghez, clarkson, tdo, morris@astro.ucla.edu

[2]Astrophysics, California Institute of Technology, MC 249-17, Pasadena, CA 91125; jlu@astro.caltech.edu, kym@caltech.edu

[3]UCLA Institute of Geophysics and Planetary Physics, Los Angeles, CA 90095-1565

[4]Space Telescope Science Institute, 3700 San Martin Drive, Baltimore, MD 21218; jayander@stsci.edu

1. Introduction

High angular resolution astrometry has been a very powerful technique for studies of the Galactic center (GC). Over the last decade, it has revealed a supermassive black hole (Eckart & Genzel 1997; Ghez et al. 1998), a disk of young stars surrounding the central supermassive black hole (Levin & Beloborodov 2003; Genzel et al. 2003; Paumard et al. 2006; Lu et al. 2009), and an eccentric orbit for the Arches, a massive young star cluster located at a projected galacto-centric distance of 30 pc (Stolte et al. 2008). While the speckle imaging work carried out on the Galactic center in the 1990's had typical centroiding uncertainties of $\sim$1 mas, recent deep, adaptive optics (AO) images have improved the precision of stellar centroiding by a factor of $\sim$6-7, significantly increasing the scientific potential of astrometry at the Galactic center (Ghez et al. 2008; Gillessen et al. 2009). Further gains in astrometric precision could lead to ultra-precise measurements of the distance to the Galactic center (R_o), measurements of individual stellar orbits at larger galacto-centric radii, and, more ambitiously, to measure post-Newtonian effects in the orbits of short-period stars (e.g., Jaroszyński 1998, 1999; Salim & Gould 1999; Fragile & Mathews 2000; Rubilar & Eckart 2001; Weinberg et al. 2005; Zucker & Alexander 2007; Kraniotis 2007; Nucita et al. 2007; Will 2008). Such gains will also probe the possibility that the supermassive black hole is moving with respect to the central stellar cluster due either to the gravitational influence of a massive companion, or from a systematic effect produced by improper alignment of images. High precision in the absolute astrometric reference frame is required in order to distinguish between these possibilities.

Two factors that currently limit astrometric measurements of stars at the Galactic center are (1) the level to which AO cameras' geometric distortions are known and (2) differential atmospheric refraction (DAR), which has not yet been explicitly corrected for in any Galactic center proper motion study (Ghez et al. 2008; Gillessen et al. 2009). While optical distortion from an infrared camera is expected to be static, distortion from the AO system and the atmosphere not corrected by AO, is not. Initial estimates of the optical distortions for AO cameras are generally based on either the optical design or laboratory test, which do not perfectly match the actual optical distortion of the system. Both uncorrected camera distortions and DAR leave $\sim$1-5 mas scale distortions over the spatial scales of the SiO masers that are used to define the absolute reference frame for proper motions of stars at the Galactic center (see e.g., Reid et al. 2007). These are significantly larger than the $\sim$0.2-0.3 mas precision achieved in the relative astrometry of Ghez et al. (2008) and Gillessen et al. (2009). While the impact of all these effects on relative astrometry has been minimized by mapping the coordinate systems of different epochs of observations to a reference set of measurements, allowing $\sim$0.2-0.3 mas precision in the relative astrometry to be achieved, the full impact of these effects is imposed on absolute astrometric measurements. Therefore, correcting these effects would have the greatest improvement on absolute astrometric

measurements. However, relative astrometry would also be improved by eliminating these effects before the images, which are obtained at different times and occasionally different orientations, are combined.

In this paper, we identify and correct for two effects that currently limit the astrometric accuracy and precision of Keck AO measurements of the Galactic center. Specifically, we (1) obtain a new, publically-available distortion solution for the infrared imaging camera behind the Keck AO system (NIRC2) and (2) correct for DAR. Furthermore, having corrected for these effects, we show that an absolute astrometric reference frame for the Galactic center can be established to within 0.3 mas/yr ($\sim$12 km/s at the distance to the GC). As an illustration of our improved reference frame, we derive a new orbit for the star, S0-2, and report on updated properties of the supermassive black hole. Section 2 presents observations and analysis of the globular cluster, M92, that were used to derive the first distortion solution for NIRC2 that is based on on-sky measurements, as opposed to NIRC2's internal pinhole mask. We present the results and tests of the distortion solution in §3. In §4 we apply this solution, along with corrections for DAR, to observations of the GC and report on our absolute astrometry as well as on the updated central potential. While this work has been carried out in the context of the Galactic center, the new distortion solution also benefits a wide array of other science that is currently being carried out with NIRC2, including astrometric studies of extrasolar planets (Marois et al. 2008), brown dwarf binaries (Konopacky et al. 2007; Liu et al. 2008; Dupuy et al. 2008), compact objects (Cameron & Kulkarni 2007), and external galaxies (e.g., Max et al. 2005).

2. Observations & Analysis

2.1. M92 (Keck)

Observations of the globular cluster M92 (NGC 6341; α = 17 17 07.27, δ = +43 08 11.5) were made from 2007 June to 2009 May using the AO system on the W. M. Keck II 10 m telescope with the facility near-infrared camera NIRC2 (PI: K. Matthews). All images were taken with the narrow field camera, which maps the 1024$\times$1024 pix array into $\sim$10"$\times$10" field of view, and through the K' (λ_0=2.12 μm, $\Delta\lambda$=0.35 μm) band-pass filter. While the Natural Guide Star adaptive optics (NGSAO) system was used to obtain the majority of the data, the Laser Guide Star (LGS) AO system was used for one run in 2008 June. The NGSAO atmospheric corrections and the LGSAO low-order, tip-tilt corrections were made using visible observations of USNO-B1.0 1331-0325486 (R = 8.5 mag). The atmospheric conditions and AO corrections for the observations yielded point spread functions (PSFs) that, on average, had Strehl ratios of $\sim$0.55 and FWHM of $\sim$50 mas.

M92 was observed at 79 different combinations of position angles (PAs) and offsets (see

Figure 1), with three identical exposures taken at each pointing. This allowed for a given star to fall on several different parts of the detector over the course of the observations. We note that the PA (θ) convention used here measures the angle (eastward) of the camera's columns with respect to North. The field of view of NIRC2's narrow camera contained the Natural Guide Star (NGS) in each pointing, and in most cases two other nearby stars, which are circled in Figure 2; this facilitated the process of combining the positional information from all of the different pointings. Empirical centroiding uncertainties are estimated using the three images at each pointing and computing the RMS error of each star's position. The typical centroiding uncertainty is $\sim$0.02 pix ($\sim$0.2 mas; see Figure 3). Table 1 provides the details of the NIRC2 M92 observations.

The M92 images are calibrated and stellar positions are measured from these images using standard techniques. Specifically, the images are first dark- and sky-subtracted, flat-fielded, and bad-pixel and cosmic ray corrected. The images are then run through the point spread function (PSF) fitting program *StarFinder* (Diolaiti et al. 2000), which is optimized for adaptive optics observations of crowded stellar fields to identify and characterize stars in the field of view. *StarFinder* iteratively constructs a PSF from a set of bright stars in the field, which have been pre-selected by the user. For M92, a total of 16 stars spread out across the detector are used to obtain a PSF that is representative of the entire field. The resulting PSF is then cross-correlated with the image and detections with a correlation peak of at least 0.7 are considered candidate stars. Relative astrometry and photometry are extracted by fitting the PSF to each candidate star. This results in a star list for each of the 237 NIRC2 images.

Final star lists for each pointing are produced by combining each set of three star lists from images with the same observational setup. Three initial criteria are used to trim out fake or problematic source detections. First, only stars detected in all three images are kept, with final positions that correspond to that from the first image. Second, we remove the two brightest stars (the NGS and a comparably bright star $\sim$5.1" to the east that appears in the images of 147 out of 237 pointings) and any other source identified within a 60-pixel ($\sim 0\farcs6$) radius of these stars (see Figure 2). These two sources are $\sim$1 mag brighter than any other detected star and are often detected at levels that saturate the detector. Saturation leads to poor PSF matching with the empirical PSF estimate, and consequently poor positional estimates for these two stars, as well as $\sim$20-50 false detections in their halos. With these selection criteria, the 79 final star lists contain a combined total of 3846 stellar position measurements of 150 independent stars.

2.2. M92 (HST ACS/WFC)

To characterize the optical distortion in the NIRC2 camera, it is ideal to compare the measured set of stellar positions to those in a distortion-free reference frame. As this idealized reference

frame does not exist, we choose observations of M92 made with the well-characterized Advanced Camera for Surveys (ACS) Wide Field Channel (WFC), which has a plate scale $\sim$49.9933 $\pm$ 0.0005 mas/pix and position angle offset = -0.0006° $\pm$ 0.0023° (van der Marel et al. 2007), as our reference frame. The distortions in this camera have been removed down to the $\sim$0.01 pix ($\sim$0.5 mas) level (Anderson 2005; Anderson & King 2006; Anderson 2007) and is therefore a useful reference for our purposes given the level of distortion in the NIRC2 camera.

HST observations of M92 were made on 2006 April 11 with both the F814W (*I*) and F606W (*V*) filters as part of the ACS Survey of Globular Clusters (GO-10775, PI: A. Sarajedini). The details of the observations, data reduction, and the construction of the M92 astrometric reference frame can be found in Anderson et al. (2008), while the catalog of positions themselves will be made available in future papers and the World Wide Web.

2.3. Galactic Center (Keck)

The images with which we derive our absolute astrometry of the Galactic center consist of five widely-dithered (6$\times$6") LGSAO data sets, three of which are described in detail in Ghez et al. (2008). These mosaics required large dithers in order to image 7 SiO masers which are used to define the absolute astrometric reference frame. Two new maser mosaics were obtained in 2008 May and 2009 June. The former mosaic was identical to the first 3, while the latter only differed in that we obtained 3 times more observations, resulting in a deeper image of $\sim$1 magnitude. The typical positional uncertainty for these mosaics was 0.52 mas. These observations are summarized in Table 2.

The observations of the central 10" of the Galaxy which are used for relative astrometry and to derive an updated orbit for S0-2 are described in detail in previous papers (Ghez et al. 2008; Lu et al. 2009) with the exception of newly obtained LGSAO data from 2008 and 2009. These data consist of speckle imaging (1995-2005) and LGSAO imaging (2004-2009), totaling 41 epochs of observation over 14 years. We obtained K' observations of the central 10" in 2008 May, 2008 July, 2009 May, 2009 July, and 2009 September, all of which were taken with identical setups to the LGSAO data described in Ghez et al. (2008). Briefly, these deep GC images were taken with the NIRC2 camera at Keck using a 20-position random dither pattern in a $0\farcs7$ box, approximately centered on Sgr A*. Typical positional uncertainties for the speckle data sets were $\sim$1 mas, while the LGSAO uncertainties were an order of magnitude more precise at 0.1 mas. This difference in the relative astrometry from the 0.2 mas reported in Ghez et al. (2008) to the 0.1 mas reported here is a result of the improvements from this work. Table 3 summarizes all the new imaging data sets of the central 10".

Three epochs of spectroscopy were also obtained in 2008 May, 2008 July, and 2009 May to add to the radial velocity measurements in Ghez et al. (2008) for S0-2. These new observations are summarized in Table 4.

3. Results

3.1. A New Distortion Solution for NIRC2

To find the best fit model for NIRC2's geometric optical distortion from the M92 observations, one must account for the fact that the ACS/WFC data do not suffer from differential atmospheric refraction (DAR; see Appendix A), while the NIRC2 data come from ground-based observations and therefore will be affected by the earth's atmosphere (see Figure 4). Differential atmospheric refraction will compress an image, causing the apparent separation between a pair of stars to be smaller than their true separation. Since the stellar positions are first geometrically distorted by the atmosphere and then the telescope/instrument, it is best to "undo" these effects in the reverse direction. During the data reduction process, it is therefore optimal to first correct for optical distortion, then remove DAR from the images before comparing with HST data. In contrast, the optical distortion should be solved for using data that still have the effects of DAR included in the images. We therefore choose to add DAR to the ACS/WFC star list. Because the effects of DAR depend on the elevation and, to a much lesser extent, the atmospheric conditions of the observations, it is necessary to create a separate DAR-transformed ACS/WFC star list for each NIRC2 star list. To account for DAR, we follow the prescription for DAR given in Gubler & Tytler (1998). The stellar positions are only corrected for achromatic DAR, as the error from chromatic DAR is negligible relative to the residual distortion in ACS/WFC ($\sim$0.5 mas). As shown in Figure 4, the magnitude of the achromatic effect over the range of elevations for the M92 observations is expected to be $\sim$2-4 mas across NIRC2's 10" field of view, along the elevation axis.

Each of the NIRC2 star lists is then used as a reference coordinate system into which the ACS/WFC star list is transformed. In the alignment process, the ACS/WFC star list is transformed by minimizing the error-weighted (NIRC2 positional errors), net displacement for all the stars, allowing for translation, rotation, and a global plate scale. This process is described in greater detail in Ghez et al. (2008) and Lu et al. (2009). Only sources that are cross-identified in both the NIRC2 and ACS star lists are used in the remaining analysis. From the 79 separate alignments, a total of 2743 matches in stellar positions are obtained for a total of 150 independent stars.

The mapping of ACS positions to NIRC2 positions shows clear spatial structure across the detector, as expected from optical distortion (see Figure 5). However, some vector deviations are inconsistent with those in their immediate surroundings. These deviant measurements are

found by examining the vector deviations in 205×205 pixel bins and determining the average and standard deviation. Any 3σ outliers in either the X or Y direction are removed. A total of 75 measurements are removed based on this criterion. An additional cut (>3σ) in each of these bins is made on NIRC2 positional uncertainties, as they may vary with respect to detector position. This cut removes 73 data points, four of which were also eliminated by the first cut. These bins are examined a second time for vector outliers, as they often show a rather wide distribution. The average and standard deviation in each bin are recalculated and the vector outliers (>3σ) are removed once again. This resulted in an additional loss of 26 measurements.

Many of the eliminated measurements come from common stars or images. We therefore remove all measurements of the 9 out of 150 stars and of the 8 out of 79 images that were eliminated more than 20% of the time by the sigma-clipping process. Many of these problematic stars have close neighbors (< 0.″2) that are not resolved or not well measured in the lower-resolution ACS observations ($\theta \sim$70 mas for the F814W observations). Similarly, the majority of the rejected frames, have exposure times less than 10 sec, while the remaining frames are at least 30 sec. This results in significantly higher centroiding uncertainties, residual atmospheric effects, and fewer stars detected. Although the 2008 April data set had relatively long exposure times (t_{int} = 48 sec), the observations were heavily impacted by clouds and the AO system was often unable to remain locked on the NGS. Our final data set consists of 2398 positional deviations between ACS and NIRC2, with typical centroiding uncertainty for the NIRC2 images of 0.02 pix ($\sim$0.2 mas). The vector plot for this cleaned sample is shown in the bottom of Figure 5.

A bivariate B-spline is fit to the distortion map (Figure 5) using the SciPy package interpolate, and a look-up table sampled at each of the 1024×1024 NIRC2 pixels is subsequently produced. The effect of the smoothing factor (f; which is related to the number of nearest-neighbor measurements used to calculate the smoothing) used in the interpolating routine was investigated extensively in order to find a good compromise between the closeness of fit and the smoothness of fit. The residuals between the original distortion vectors in the bottom panel of Figure 5 and the computed shift at the nearest pixel (from the smoothed look-up table) were measured. The median deviation is found to increase until $f \sim$150, where it plateaus at a value of $\sim$0.27 pix. We choose for our interpolation the smoothing factor that gave nearly the lowest median deviation, f = 135. Although the deviations were lower for distortion solutions created with smaller smoothing factors, the edge effects were prominent in the look-up tables and the distribution of deviations was much larger (see Dierckx (1995) for details on surface fitting and the choice of smoothing factors). The resulting look-up tables for shifts in X and Y are shown in Figure 6, and are produced in the form of FITS files that may be fed into the IRAF routine, *Drizzle* (Fruchter & Hook 2002), to correct for the optical distortion. Figure 7 shows a histogram of these values.

Uncertainties in the distortion solution were computed by running 1000 Monte Carlo sim-

ulations, in which the data were sampled with replacement. The RMS error with respect to the distortion solution (i.e., the actual distortion solution was taken as the average) was calculated at each pixel and the results are shown in the bottom of Figure 6. The average errors in X and Y are 0.05 pix and 0.04 pix ($\sim$0.4, $\sim$0.5 mas), respectively. We can see the uncertainties are highest near the edge of the detector, where less data exist. The uncertainties are also shown in the form of a histogram in Figure 7 along with a histogram of the distortion solution itself.

To solve for the global plate scale and orientation that results from this new solution, we re-reduce the raw NIRC2 observations of M92 from 2007 July, and apply corrections for distortion and DAR to these images. The distortion correction and DAR correction are applied to each image at the same time in the form of look-up tables using the *Drizzle* algorithm as implemented in IRAF (Fruchter & Hook 2002). The look-up tables are specified in *Drizzle* using the *xgeoim* and *ygeoim* keywords and are FITS files of the same dimensions as the science image. Because DAR depends on the zenith angle and atmospheric conditions, both of which vary in time, the look-up tables are created by first including the distortion solution and then applying the necessary DAR correction. Two FITS files, one for shifts in X and one for shifts in Y, are created for each NIRC2 observation and contain the shifts to be applied to each pixel in the image. From these distortion- and DAR-corrected NIRC2 images, star lists were generated and aligned to the original ACS starlist (without DAR) as described above. The resulting plate scale is $\langle s \rangle = 9.948 \pm 0.001_{stat} \pm 0.001_{abs}$ $\mathrm{pix}_{NIRC2}/\mathrm{pix}_{ACS/WFC}$. The difference between the orientation given in the header of the NIRC2 images[1] (90° for this data set) and the measured orientation is on average $\sim 0.256° \pm 0.006°_{stat} \pm 0.002°_{abs}$, where the absolute errors are the RMS uncertainties in the ACS/WFC plate scale and orientation angle (van der Marel et al. 2007). Thus, the NIRC2 columns must be rotated eastward of North by 0.256° to be aligned with ACS.

3.2. Testing the New Model for NIRC2 Distortion

The accuracy of our distortion solution is examined using two separate LGSAO GC data sets, both of which are described in Ghez et al. (2008), and compared with two previous estimates, which we refer to as "pre-ship" and "PBC". The pre-ship solution[2], which is good to $\sim$4 mas, was found using a pinhole mask, and is in the form of a 3rd-order polynomial. The more recent solution by P. B. Cameron, also from a pinhole mask, is a 4th-order polynomial and improves upon

[1]The NIRC2 FITS header keyword for the position angle, ROTPOSN, includes a +0.7° offset (given by header keyword INSTANGL), the observatory value for the angle offset of NIRC2. The nominal position angle for NIRC2 in our analysis is taken as (ROTPOSN - INSTANGL).

[2]http://www2.keck.hawaii.edu/inst/nirc2/preship_testing.pdf

the former solution mainly along the X axis[3].

First, we use the two high precision data sets taken of the central 10"×10" on 2007 May 17 and May 20 at two different PAs (0° and 200°) with roughly the same central position. The NIRC2 positional uncertainties (δ_{pos}) for the PA=0 and PA=200 images are ∼0.022 pix and ∼0.036 pix, respectively. The PA=200 image was transformed into the PA=0 image's coordinate system, again allowing for translation, rotation, and global plate scale. The differences in the aligned positions of stars with K<14.5 are shown in Figure 8. This comparison gives an average residual distortion by comparing the positions of a star at two distinct locations on the detector. Our new solution shows significantly less residual structure than the previous solutions. To estimate the magnitude of the residual distortion, we remove the positional measurement bias and account for the contribution from the two images used:

$$\sigma_r = \sqrt{\frac{\Delta_{2D}^2 - \delta_{pos,0}^2 - \delta_{pos,200}^2}{2}} \quad (1)$$

where Δ_{2D} is the measured positional offset between the two images. This results in estimates of the residual distortion, of σ_r = 0.11 pix, 0.23 pix, and 0.24 pix for the new, PBC, and pre-ship solutions, respectively.

To characterize the residuals in X and Y separately so that we can compare to values from previous distortion solutions, we use widely-dithered GC data taken in 2008 May at PA=0, which maintains the independence of the X and Y axes. Largely-dithered data sets are essential in testing the distortion solution because stars are placed on very different locations on the distortion map, and therefore provide a sensitive test of residual distortion. These data are described in Ghez et al. (2008) as part of their absolute astrometry analysis and have an average centroiding uncertainty of 0.067 pix. Only four overlapping fields, each of which was imaged three times and whose centers are the corners of a 6"×6" box, were examined from this data set. The full mosaic is shown in Figure 9. *StarFinder* was run at a correlation of 0.9 on each image to create a star list, and only stars detected in at least 6 of the 12 images (and therefore at least two of the four overlapping fields) were kept in the analysis. The variance of each star's offsets (Δx_i and $\Delta_i y$) from IRS16SW-E (which was in each of the four fields) was computed as:

$$\sigma_{x,i}^2 = \frac{\sum(\Delta x_i - \langle \Delta x_i \rangle)^2 - (\delta_{pos,IRS16SWE}^2 + \delta_{pos,i}^2)}{2(N_{fields} - 1)} \quad (2)$$

and likewise for σ_y, where we divide by the number of overlapping fields in which a star was detected (N_{fields}), and we have corrected for the NIRC2 positional measurement bias (δ_{pos}) for both IRS16SW-E and star *i*. The factor of 2 in the denominator accounts for the fact that the distortion

[3]http://www.astro.caltech.edu/∼pbc/AO/distortion.pdf

affects both stars, IRS16SW-E and star *i*. The RMS offsets (σ_x, σ_y) for these solutions, shown in Figure 10, are (0.09, 0.13) pix, (0.10, 0.27) pix, and (0.35, 0.30) pix, for the new, PBC, and pre-ship solutions, respectively. The new solution was found to significantly improve positional errors overall as compared to both of the previous solutions and in particular, it is a factor of 2 better in the Y direction over the more recent PBC solution.

3.3. Additional Sources of Uncertainty

While the new distortion solution represents a significant step forward in our astrometric capabilities, it still leaves $\sim$0.1 pix or $\sim$1 mas residual distortion in the LGSAO GC images. The residual distortion is $\sim$2.5 times larger than our estimated uncertainties ($\sim$0.05 pix; Figure 7), and must come from sources of uncertainty that are not accounted for in our analysis. These may include source confusion in the ACS/WFC positions, residual distortion in the ACS/WFC camera, unaccounted for PSF spatial dependencies in the NIRC2 images, chromatic DAR, time-variable distortion, or a difference between NGSAO and LGSAO data.

To test the stability of the camera's distortion, we created a distortion solution with data points from 2007, the year with the most data (N=1711). A smoothing factor of f = 120 was used for the spline fitting and was determined in the same manner as our new distortion solution. Differences between the 2007-only distortion solution and the data in the individual years show no significant differences (0.01$\pm$0.22 pix, 0.05$\pm$0.30 pix, and 0.09$\pm$0.29 pix for 2007, 2008, and 2009, respectively), suggesting that the distortion solution is relatively stable.

While we tested our distortion solution on LGSAO data, the model itself was computed using only NGS data, as the six LGS frames from 2008 June were thrown out based on the cuts mentioned in §3.1. To test the possibility that the NGS and LGS AO system have different distortion solutions, we compare Galactic center data taken in both LGS and NGS modes, but otherwise the same setup and in the same night in 2008 May. The data were reduced using the usual data reduction steps (see Ghez et al. (2008)), and final LGS- and NGS-only images of the Galactic center were produced. The astrometric precision for each of these images was 0.018 pix (NGS) and 0.021 pix (LGS) for stars with K < 15. The LGS image was transformed into the NGS image's coordinate system allowing only for translation between the two frames. The RMS difference in the aligned positions was $\sim$0.06 pix (1σ), which is comparable to the error in the distortion solution ($\sim$0.05 pix, Figure 7). Thus, given the uncertainties in the distortion solution, we do not see a difference in the astrometry from images taken in NGS or LGS mode and conclude that this adds only a small contribution to the residual distortion.

The residual distortion (0.15 pix) may be included as a constant term in the error map of the

distortion (see §3.1) when analyzing astrometric data. We choose to add this to the errors in the mosaic distortion map when determining the positions of the SiO masers in the Galactic center (see §4.1).

4. Application to the Galactic Center

4.1. Absolute Astrometric Reference Frame

In this section, we compare our observations of SiO masers to measurements that have been made at radio wavelengths in a SgrA*-radio rest frame (Reid et al. 2003, 2007) as another check of the accuracy of our distortion model and DAR corrections, as well as to derive a new and substantially improved IR *absolute* reference frame. We use the data sets presented in Table 2 for this analysis. In each of the five epochs, a mosaic was constructed in the same way described in Ghez et al. (2008), which combines the images collected at nine different pointings and which results in 22"$\times$22" images (see Figure 9). *StarFinder* was run on each IR mosaic to create a star list for each epoch with positions in NIRC2 pixel coordinates. Along with this, we also constructed a corresponding distortion uncertainty map based on a mosaic of the distortion uncertainty maps from the Monte Carlo simulations (§3.1; Figure 6) and thereby calculated the distortion error contribution to each pixel in the maser mosaic. In the overlapping areas, we compute the distortion error contribution as

$$\sigma_{dist} = \sqrt{\frac{\sigma_1^2 + \sigma_2^2 + ... + \sigma_N^2}{N}} \quad (3)$$

where N is the number of overlapping fields, which can vary between 1 and 4. The IR uncertainties in each mosaic's star list include the centroiding error, distortion error, and the residual distortion ($\sim$0.15 pix), summed in quadrature. Radio maser positions were propagated forward using velocities from Reid et al. (2007) to create a star list at the epoch of each IR mosaic. Each of the five infrared mosaics was aligned with a four-parameter model (two-dimensional translation, rotation, and a single pixel scale) to the radio maser star list by minimizing the error-weighted, net displacements for the masers. Errors in the transformation to absolute coordinates were determined using a jack-knife sampling technique, in which one maser at a time is excluded from the alignment. Since all the transformed IR positions agree with the radio positions to within $\sim 1\sigma$ of each other and the alignment uncertainties[4] are negligible, we are confident that our uncertainties are well characterized and we are not missing large systematic error sources. The various sources of error in our absolute astrometry are broken down in Table 5. Similar NIRC2 pixel scale and orientation values are obtained from the SiO maser alignment, on average, as compared to those

[4]RMS error of individual positions in jack-knife MC simulations of transformation process.

obtained from the M92 study (Table 6). We note, however, that the orientation shows a larger RMS scatter between the epochs than the average of the uncertainty inferred from the jack-knife analysis of each epoch (0.01° vs 0.003°) and the pixel scale also shows an increase, although much smaller (0.002 vs. 0.001 mas/pix). We therefore take the RMS values as our estimates of the uncertainties for our final values of the pixel scale and orientation angle given in Table 6. The weighted average NIRC2 plate scale and angle offset from the IR to radio alignments are 9.953 ± 0.002 mas/pix and $0.252 \pm 0.012°$, respectively. These are statistically consistent with the values obtained from the ACS/WFC to NIRC2 transformation from the 2007 July M92 data set (§3.1). We take the average of these measurements as our final values for the NIRC2 pixel scale and orientation angle, 9.951 $\pm$ 0.003 mas/pix and $0.252 \pm 0.013°$, respectively.

Our transformed IR mosaic maps provide a calibrated astrometric reference frame in which Sgr A* is at rest at the origin. Comparison of the SiO masers as measured in the IR and radio provide estimates of how well we can localize the position and velocity within this reference frame. Figure 11 shows the positions of the SiO masers measured in the IR and radio for the 2007 August epoch (other epochs gave very similar results). Line fits between these two positional measurements, weighted by the positional errors in both the IR and radio, suggest that we can localize Sgr A* in any of these reference frames to $\sim$1.6 mas and $\sim$2.1 mas in X and Y, respectively. These values are the formal intercept errors from the weighted line fits. Among the 7 SiO masers used, 5 have total positional uncertainties that are larger in the IR than in the radio, as shown in Table 5. These stem mostly from uncertainties in the distortion model and can therefore be improved through more extensive modeling efforts and by mapping the SiO masers in multiple setups. We however note that more radio measurements are needed to prevent these positional uncertainties from overtaking the infrared positional uncertainties in the future. Our current uncertainties for the position of Sgr A* are a factor of $\gtrsim$2 better than that obtained in our earlier efforts (Ghez et al. 2008), when treated in the same manner[5] and comparable to the uncertainties reported in Gillessen et al. (2009).

For each maser, the absolute velocity was calculated by fitting a line to the star's transformed position as a function of time, weighted by the positional uncertainties. The uncertainties in the fit parameters are determined from the covariance matrix. The results of these line fits are summarized in Table 7, where the positions and velocities are given for a reference time, T_0, which is the mean of the time for all epochs weighted by the maser's positional uncertainty. The fits for each maser are shown in Figures 12 and 13, along with the radio positions which have been propagated to the IR mosaic's epoch using the proper motions from Reid et al. (2007). A comparison of the IR and radio proper motions (Figure 14) provide estimates of how well an absolute IR reference frame

[5]We reported absolute errors from a half-sample bootstrap in Ghez et al. (2008). To compare values we reran the half-sample bootstrap, which overestimates the uncertainties since half the sample is removed.

can be established in velocity space. A linear fit to these data, weighted by the velocity errors in both the IR and radio, gives a slope and intercept of 1.12 $\pm$ 0.15 and -0.17 $\pm$ 0.26 mas/yr in the X direction, and 0.95 $\pm$ 0.10 and -0.12 $\pm$ 0.38 mas/yr in the Y direction. As with our analysis on the absolute positions, the errors are the formal uncertainties from the line fits. The intercept errors of these lines reflect our ability to define an astrometric reference frame, and we conclude that this can be done to better than $\sim$0.4 mas/yr, which is a factor of $\sim$3 improvement over earlier work (Ghez et al. 2008).

4.2. Relative Motion Between Sgr A* and Stellar Cluster

The relative astrometry of the Galactic center was derived using all data sets of the central 10" of the Galaxy, which are comprised of speckle and LGSAO imaging. The data reduction and analysis procedure are also described in Ghez et al. (2008) but we note that we used the new distortion solution and corrected for DAR in this analysis. In order to combine existing Galactic center data sets from NIRC (1995-2004) and NIRC2 (2004-2009), the NIRC distortion solution was rederived using methods described in Lu et al. (2009). The new NIRC distortion solution coefficients are presented in Table 8 and should be used in place of those in Table 5 of Lu et al. (2009).

The relative reference frame for the Galactic center is established by aligning the IR images to each other using a set of "coordinate reference" stars. This procedure effectively puts the stellar cluster at rest. Star lists from each epoch were transformed into the 2007 August data set's coordinate system, and linear models were fit to the stars' positions as a function of time. These relative astrometric measurements were transformed into the absolute reference frame using a set of *infrared absolute astrometric standards*. These standards were defined as stars that (1) are detected in all 5 maser mosaics, (2) are outside the central arcsecond (r > 0.5") to reduce the effects of non-linear motions over time, (3) are brighter than K=15, (4) have velocities below 15 mas/yr and velocity errors below 5 mas/yr, (5) have reasonable velocity fits (χ^2/dof) < 4 (Ghez et al. 2008), and (6) have been identified as late-type stars by Do et al. (2009) and Buchholz et al. (2009). This last criterion is used in order to eliminate the known net-rotation of the young stars (Genzel et al. 2000). The average positional uncertainty for these astrometric standard stars is 0.9 mas.

The stars' proper motions as measured in the radio reference frame (*absolute*) can be compared to their proper motions measured in the infrared frame (*relative*) in order to determine whether there is relative motion between the two. Since Sgr A* is defined to be at rest in the radio reference frame, a velocity difference between the absolute and relative reference frames may imply that either Sgr A* is moving with respect to the cluster, or the cluster itself has a non-zero net motion. Thus, this is an additional technique for examining the apparent motion of Sgr

A* relative to the cluster (Ghez et al. 2008) and for comparing with the dynamical center velocity as derived from the orbit of S0-2 (§4.3).

Figure 15 shows the difference between absolute and relative velocities for 203 stars matched across the two reference frames. The outliers in the velocity differences are due to stars at relatively large distances (r $\gtrsim$ 5") from Sgr A*. The average of the velocity differences is (for X and Y, respectively) 0.2 $\pm$ 0.4 and 0.3 $\pm$ 0.6 mas/yr, where the uncertainties are the standard deviation of the velocity differences and are comparable to the errors in the proper motions measured in the radio ($\sim$0.4 mas/yr) implying that the IR measurements are limited by the radio. The distribution of velocity differences in the North-South direction is slightly offset from zero likely due to residual distortion, which becomes most apparent when using such widely-dithered data sets. We conclude that we do not detect a significant motion between the stellar cluster and the black hole.

4.3. Orbit of S0-2

The stellar orbit of S0-2 was derived using 29 epochs of imaging data and 16 epochs of spectroscopic data, as well as five additional epochs of radial velocity measurements reported in the literature (Eisenhauer et al. 2003, 2005). These observations are summarized in Ghez et al. (2008) and in our Tables 3 and 4. We note that in this new analysis, S0-2's astrometric data points in 2006 June and 2006 July are biased by S0-20, which is not detected in either of these epochs by *StarFinder*. We thus exclude these points from our analysis (see Ghez et al. (2008) for details on astrometric biases). As done previously, we also removed biased astrometric data points from 1998 (due to confusion with S0-19), from 2002 (due to overlap with Sgr A*), and from 2007 May (due to superposition with S0-20).

The relative positions of S0-2 were placed into the absolute coordinate reference frame described above. The orbital analysis on these positions was carried out in an identical fashion to the 13-parameter fit in Ghez et al. (2008) but we summarize the important steps of the analysis here. The properties of the black hole that are fit for in this analysis are the mass (M), distance (R_0), location on the plane of the sky (X_0, Y_0), and motion (V_x, V_y, V_z). Thus, no priors are imposed on the black hole's motion. The six orbital elements of S0-2, which are also free parameters in this fit are: period (P), eccentricity (e), time of periapse passage (T_0), inclination (i), position angle of the ascending node (Ω), and the longitude of periapse (ω). Monte Carlo simulations were used to estimate the uncertainties in these fitted parameters, as described in Ghez et al. (2008).

The astrometric and radial velocity data are listed in Tables 9 and 10, and shown in Figure 16, with the best-fit Keplerian model overplotted. This best fit orbit has a total χ^2 of 77.5 for 66 degrees of freedom, resulting in a reduced χ^2 of 1.174. Probability distributions for the black hole's mass

and distance were derived from the Monte Carlo simulations and are shown in Figure 17. We find a best fit for the black hole's mass of M_{BH} = 4.1 $\pm$ 0.4 $\times$ 10^6 $M_\odot$ and distance of R_0 = 8.0 $\pm$ 0.4 kpc, where the uncertainties quoted are 1σ values. The derived values of the potential and the orbital elements of S0-2 are shown in Table 11 and are consistent with the Ghez et al. (2008) results.

The most notable differences between the orbit of S0-2 in this work and that of Ghez et al. (2008) are the position and velocity of the dynamical center. We find for the location of the dynamical center ($X_0 - X_{SgrA^*}$) = 3.0 $\pm$ 1.0 mas, ($Y_0 - Y_{SgrA^*}$) = -2.0 $\pm$ 1.4 mas, while for the velocity of Sgr A* relative to the stellar cluster we estimate V_x = 0.13 $\pm$ 0.10 mas/yr, V_y = -0.05 $\pm$ 0.12 mas/yr, and V_z = -21 $\pm$ 20 km/s. Therefore, we do not detect a significant relative motion between the black hole and the stellar cluster, consistent with the analysis in section 4.1.

We repeated this exercise with the 2008 and 2009 data points (astrometry and radial velocities) excluded in order to verify that the differences between the results in this work and those in Ghez et al. (2008) are not due to the addition of our newly obtained data. We find a best fit orbit with a reduced χ^2 of 1.191. The orbital elements and properties of the potential are consistent with the orbit we obtained when including the new data to within 1σ. Thus, we attribute the differences to the new techniques and analysis in this work.

5. Conclusions

We have improved upon existing geometric distortion solutions for the NIRC2 camera at the W. M. Keck II telescope and have, for the first time, implemented DAR corrections to our Galactic center astrometry. In all tests that were performed, the new distortion solution shows an improvement by a factor of $\sim$2-4 over existing solutions. We take as our final residuals: (Δx_{rms}, Δy_{rms}) $\sim$ (0.09, 0.13) pix. The transformations between the ACS/WFC and NIRC2 reference frames yield a consistent plate scale and angle offset to that obtained using Galactic center infrared data which are tied to the radio reference frame. We find an average plate scale and angle offset for the NIRC2 narrow camera of 9.951 $\pm$ 0.003 mas/pix and 0.252 $\pm$ 0.013°, respectively.

The Galactic center astrometry can now be tied to an absolute reference frame to better than $\sim$1.5 mas and $\sim$0.4 mas/yr in position and velocity space, respectively, as a result of this work. The stellar orbit for S0-2 within this improved reference frame results in a mass of and distance to the supermassive black hole of M_{BH} = 4.1 $\pm$ 0.4 $\times$ 10^6 $M_\odot$, and R_0 = 8.0 $\pm$ 0.4 kpc, respectively, which is fully consistent with the results of Ghez et al. (2008). Furthermore, we find no net relative motion between the stellar cluster and the central black hole.

Improvements to the NIRC2 distortion solution may be made by increasing the number of positional measurements used to derive the solution in order to more fully sample the detector.

Another source of error in our solution is the residual distortion in ACS/WFC ($\sim$0.5 mas), and thus a self-calibrated NIRC2 distortion solution (Anderson & King 2003) may improve the solution further. The use of a single point spread function across the field is also a rather significant source of error, as the quality of the AO correction is best at the location of the laser and gets worse further away, leading to a spatially-variable PSF. Assuming a uniform PSF will therefore cause errors in positional measurements. To minimize this effect, we are currently developing an algorithm to create a location-dependent point spread function.

The new distortion solution, in the form of two FITS files, may be obtained at http://www.astro.ucla.edu/$\sim$ghezgroup/distortion or by emailing the first author. The FITS files, or look-up tables, may be fed into the IRAF routine *Drizzle* during the data reduction process. The values in the look-up tables specify the shifts required to put an image in a "distortion-free" reference frame. The errors in the distortion solutions may also be obtained at this site.

We thank the staff of the Keck Observatory, especially Randy Campbell, Al Conrad, Jim Lyke, and Hien Tran for their help in obtaining the observations. We also thank Quinn Konopacky and Leo Meyer for their helpful suggestions on this work and the manuscript. Support for this work was provided by the NSF grant AST-0406816 and the NSF Science & Technology Center for Adaptive Optics, managed by UCSC (AST-9876783). The W. M. Keck Observatory is operated as a scientific partnership among the California Institute of Technology, the University of California and the National Aeronautics and Space Administration. The Observatory was made possible by the generous financial support of the W. M. Keck Foundation.

Facilities: Keck: II (NIRC2)

REFERENCES

Anderson, J. 2005, in The 2005 HST Calibration Workshop Proceedings, ed. A. Koekemoer, P. Goudfrooij, & L. L. Dressel, 11–20

Anderson, J. 2007, Variation of the Distortion Solution, Tech. rep.

Anderson, J., & King, I. R. 2003, PASP, 115, 113

—. 2006, PSFs, Photometry, and Astronomy for the ACS/WFC, Tech. rep.

Anderson, J., Sarajedini, A., Bedin, L. R., King, I. R., Piotto, G., Reid, I. N., Siegel, M., Majewski, S. R., Paust, N. E. Q., Aparicio, A., Milone, A. P., Chaboyer, B., & Rosenberg, A. 2008, AJ, 135, 2055

Buchholz, R. M., Schödel, R., & Eckart, A. 2009, AAP, 499, 483

Cameron, P. B., & Kulkarni, S. R. 2007, in Bulletin of the American Astronomical Society, Vol. 38, Bulletin of the American Astronomical Society, 996–+

Dierckx, P. 1995, Curve and Surface Fitting with Splines (Oxford University Press)

Diolaiti, E., Bendinelli, O., Bonaccini, D., Close, L., Currie, D., & Parmeggiani, G. 2000, A&AS, 147, 335

Do, T., Ghez, A. M., Morris, M. R., Lu, J. R., Matthews, K., Yelda, S., & Larkin, J. 2009, ArXiv e-prints

Dupuy, T. J., Liu, M. C., & Ireland, M. J. 2008, ArXiv e-prints

Eckart, A., & Genzel, R. 1997, MNRAS, 284, 576

Eisenhauer, F., Genzel, R., Alexander, T., Abuter, R., Paumard, T., Ott, T., Gilbert, A., Gillessen, S., Horrobin, M., Trippe, S., Bonnet, H., Dumas, C., Hubin, N., Kaufer, A., Kissler-Patig, M., Monnet, G., Ströbele, S., Szeifert, T., Eckart, A., Schödel, R., & Zucker, S. 2005, ApJ, 628, 246

Eisenhauer, F., Schödel, R., Genzel, R., Ott, T., Tecza, M., Abuter, R., Eckart, A., & Alexander, T. 2003, ApJL, 597, L121

Fragile, P. C., & Mathews, G. J. 2000, ApJ, 542, 328

Fruchter, A. S., & Hook, R. N. 2002, PASP, 114, 144

Genzel, R., Pichon, C., Eckart, A., Gerhard, O. E., & Ott, T. 2000, MNRAS, 317, 348

Genzel, R., Schödel, R., Ott, T., Eisenhauer, F., Hofmann, R., Lehnert, M., Eckart, A., Alexander, T., Sternberg, A., Lenzen, R., Clénet, Y., Lacombe, F., Rouan, D., Renzini, A., & Tacconi-Garman, L. E. 2003, ApJ, 594, 812

Ghez, A. M., Klein, B. L., Morris, M., & Becklin, E. E. 1998, ApJ, 509, 678

Ghez, A. M., Salim, S., Weinberg, N. N., Lu, J. R., Do, T., Dunn, J. K., Matthews, K., Morris, M., Yelda, S., Becklin, E. E., Kremenek, T., Milosavljevic, M., & Naiman, J. 2008, ApJ, In press

Gillessen, S., Eisenhauer, F., Trippe, S., Alexander, T., Genzel, R., Martins, F., & Ott, T. 2009, ApJ, 692, 1075

Gubler, J., & Tytler, D. 1998, PASP, 110, 738

Jaroszyński, M. 1998, Acta Astronomica, 48, 413

—. 1999, ApJ, 521, 591

Konopacky, Q. M., Ghez, A. M., Duchêne, G., McCabe, C., & Macintosh, B. A. 2007, AJ, 133, 2008

Kraniotis, G. V. 2007, ArXiv e-prints

Lazorenko, P. F. 2006, AAP, 449, 1271

Lazorenko, P. F., Mayor, M., Dominik, M., Pepe, F., Segransan, D., & Udry, S. 2007, AAP, 471, 1057

Levin, Y., & Beloborodov, A. M. 2003, ApJL, 590, L33

Liu, M. C., Dupuy, T. J., & Ireland, M. J. 2008, ApJ, 689, 436

Lu, J. R. 2008, Ph.D. Thesis

Lu, J. R., Ghez, A. M., Hornstein, S. D., Morris, M. R., Becklin, E. E., & Matthews, K. 2009, ApJ, 690, 1463

Marois, C., Macintosh, B., Barman, T., Zuckerman, B., Song, I., Patience, J., Lafrenière, D., & Doyon, R. 2008, Science, 322, 1348

Max, C. E., Canalizo, G., Macintosh, B. A., Raschke, L., Whysong, D., Antonucci, R., & Schneider, G. 2005, ApJ, 621, 738

Nucita, A. A., De Paolis, F., Ingrosso, G., Qadir, A., & Zakharov, A. F. 2007, PASP, 119, 349

Paumard, T., Genzel, R., Martins, F., Nayakshin, S., Beloborodov, A. M., Levin, Y., Trippe, S., Eisenhauer, F., Ott, T., Gillessen, S., Abuter, R., Cuadra, J., Alexander, T., & Sternberg, A. 2006, ApJ, 643, 1011

Reid, M. J., Menten, K. M., Genzel, R., Ott, T., Schödel, R., & Eckart, A. 2003, ApJ, 587, 208

Reid, M. J., Menten, K. M., Trippe, S., Ott, T., & Genzel, R. 2007, ApJ, 659, 378

Rubilar, G. F., & Eckart, A. 2001, AAP, 374, 95

Salim, S., & Gould, A. 1999, ApJ, 523, 633

Stolte, A., Ghez, A. M., Morris, M., Lu, J. R., Brandner, W., & Matthews, K. 2008, ApJ, 675, 1278

van der Marel, R. P., Anderson, J., Cox, C., Kozhurina-Platais, V., Lallo, M., & Nelan, E. 2007, Calibration of ACS/WFC Absolute Scale and Rotation for Use in creation of a JWST Astrometric Reference Field, Tech. rep.

Weinberg, N. N., Milosavljević, M., & Ghez, A. M. 2005, ApJ, 622, 878

Will, C. M. 2008, ApJL, 674, L25

Zucker, S., & Alexander, T. 2007, ApJL, 654, L83

A. Differential Atmospheric Refraction

A pair of stars viewed through the Earth's atmosphere will have different separations depending on the zenith angle at which they are viewed. This effect is due to differential atmospheric refraction (DAR) and is described in detail in Gubler & Tytler (1998), Lazorenko (2006), and Lazorenko et al. (2007)[6]. There is both chromatic and achromatic differential atmospheric refraction; however, the achromatic term is at least 20 times larger than the chromatic term (Gubler & Tytler 1998). Sources at the Galactic center have similar colors due to the high extinction and, as a result, the chromatic term is negligible. Color differences for stars in M92, however, may result in small residual systematic errors ($\sim$0.2 mas) in our comparison of ground-based to space-based astrometry due to chromatic DAR, but this effect is smaller than the residual distortion in ACS/WFC ($\sim$0.5 mas). Therefore, the stellar positions in this work are only corrected for achromatic DAR.

The true angular separation of two stars along the zenith direction, $\Delta z = z_1 - z_2$, is modified by differential atmospheric refraction such that the observed angular separation becomes $\Delta z_{obs} = \Delta z_{true} - \Delta R$. Neglecting chromatic effects, the DAR term (ΔR) depends only on (1) the observed zenith angle of star 1, (2) the wavelength of the observations, (3) the observed zenith separation of star 1 and star 2, (4) the temperature at the observatory, (5) the pressure at the observatory, and (6) the relative humidity at the observatory. The atmospheric parameters of interest are downloaded from an archive maintained at the Canada-France-Hawaii Telescope (CFHT)[7]. These values are recorded every five minutes, allowing us to find the appropriate atmospheric conditions

---

This preprint was prepared with the AAS LaTeX macros v5.2.

[6]See also Evans, D. W., "Atmospheric Differential Refraction in the Infrared", 2004, `http://www.ast.cam.ac.uk/vdfs/documentation.html`

[7]`http://kiloaoloa.soest.hawaii.edu/archive/wx/cfht/`

on Mauna Kea within three minutes of the observation (Lu 2008). During our observations, the typical atmospheric conditions at night on Mauna Kea have a temperature of 272 K, a relative humidity of 10%, and a pressure of 617 millibars. Figure 4 shows, for these typical conditions, the magnitude of DAR. We also show the actual magnitude of the effect for the individual images as points along the 10" case, showing that the variations in conditions do not have a significant effect on DAR.

Table 1. Summary of M92 Images

Date[a] (UT)	PA (deg)	$(X,Y)_{GS}$[b] (pix)	$\Delta(X,Y)$[c] (pix)	El (deg)	Temp (K)	Pressure (mbar)	RH[d] %	ΔR[e] (mas)	$t_{exp,i} \times$coadd (sec)	$\langle$FWHM$\rangle$ (mas)	$\langle$Strehl$\rangle$	N stars detected	N stars used	$\langle\sigma_{pos}\rangle$[f] (pix)
2007 June 21	0	508, 512	0, 0	53	271.2	616.8	92	2.74	3.0×10	49	0.55	105	69	0.037
			254, -252	53	271.1	616.7	89	2.77		48	0.55	145	58	0.035
			251, 252	52	271.1	616.7	89	2.81		48	0.57	112	46	0.045
			-251, -252	52	271.3	616.7	93	2.84		48	0.59	176	56	0.034
			-253, 250	51	271.3	616.7	93	2.89		49	0.54	110	57	0.037
			251, 0	51	271.2	616.7	95	2.93		48	0.60	124	58	0.044
			-251, -1	50	271.2	616.7	95	2.97		47	0.59	115	64	0.049
			2, -250	50	271.1	616.7	96	3.02		47	0.58	124	47	0.063
			0, 253	49	271.0	616.6	97	3.07		46	0.61	94	51	0.058
2007 July 29	90	457, 499	0, 0	67	272.9	615.3	11	2.07	0.8×60	45	0.64	73	47	0.031
			255, -251	67	272.9	615.3	11	2.07		45	0.72	53	38	0.048
			251, 255	67	272.9	615.3	12	2.07		45	0.68	84	41	0.042
			-249, -251	67	272.9	615.2	12	2.07		46	0.66	65	40	0.052
			-252, 251	67	272.9	615.2	13	2.07		45	0.69	132	52	0.031
			254, 2	67	272.9	615.3	13	2.07		45	0.71	72	44	0.021
			-252, 0	66	272.9	615.2	13	2.08		45	0.72	93	48	0.037
			3, -250	66	272.8	615.2	12	2.09		44	0.73	69	47	0.029
			-2, 253	66	272.8	615.2	12	2.10		45	0.72	92	51	0.024
			-125, -124	65	272.8	615.2	12	2.11		45	0.72	85	50	0.026
			128, -375	65	272.8	615.2	13	2.12		45	0.73	89	48	0.030
			126, 129	65	272.8	615.2	12	2.14		45	0.70	84	54	0.030
			-374, -376	64	272.8	615.2	13	2.16		46	0.69	47	33	0.033
			-378, 126	64	272.8	615.2	12	2.18		46	0.68	74	39	0.067
			128, -123	63	272.9	615.2	12	2.20		46	0.67	77	49	0.038
			-374, -125	62	272.9	615.2	12	2.22		46	0.67	72	38	0.032
			-121, -374	62	272.9	615.2	12	2.25		46	0.67	51	38	0.028
			-127, 129	61	273.0	615.2	11	2.27		46	0.66	87	45	0.045
			127, -121	60	273.1	615.1	11	2.31		46	0.65	81	47	0.045
			380, -373	60	273.2	615.1	12	2.34		47	0.63	52	33	0.071
			378, 132	59	273.1	615.1	12	2.38		46	0.65	51	39	0.025
			-126, -373	58	273.3	615.1	12	2.41		46	0.66	54	36	0.032
			-128, 130	57	273.3	615.1	11	2.46		47	0.65	76	45	0.031
			381, -120	56	273.3	615.0	11	2.50		47	0.64	43	35	0.040

Table 1—Continued

Date[a] (UT)	PA (deg)	$(X,Y)_{GS}$[b] (pix)	$\Delta(X,Y)$[c] (pix)	El (deg)	Temp (K)	Pressure (mbar)	RH[d] %	ΔR[e] (mas)	$t_{exp,i} \times$coadd (sec)	$\langle$FWHM$\rangle$ (mas)	$\langle$Strehl$\rangle$	N stars detected	N stars used	$\langle\sigma_{pos}\rangle$[f] (pix)
			-127, -120	56	273.4	615.0	10	2.55		47	0.61	64	43	0.022
			129, -371	55	273.3	615.0	12	2.60		47	0.63	54	39	0.040
			124, 133	54	273.3	614.9	11	2.66		48	0.60	79	47	0.036
2008 Apr 28	180	496, 477	0, 0	67	271.0	615.8	82	2.08	0.8×60	47	0.56	31	20	0.022
			252, -252	67	271.0	615.7	81	2.08		48	0.53	32	0	-1.000
			248, 253	67	271.0	615.8	83	2.08		48	0.55	55	15	0.061
			113, -375	63	271.5	616.0	70	2.23		48	0.54	12	0	-1.000
			-143, -120	59	271.0	616.0	77	2.39		51	0.44	13	9	0.022
2008 June 3	0	776, 573	0, 0	42	273.3	616.0	64	3.85	1.5×6	50	0.47	30	0	-1.000
			4, 4	42	273.2	616.1	65	3.89		51	0.48	32	0	-1.000
			-4, 0	42	273.2	616.1	65	3.93		58	0.29	29	0	-1.000
			4, 0	41	273.2	616.1	65	3.97		54	0.38	32	0	-1.000
			-4, 3	41	273.2	616.1	65	4.01		54	0.38	25	0	-1.000
			-5, -4	41	273.2	616.1	65	4.05		54	0.40	26	0	-1.000
2008 July 24	45	173, 565	0, 0	50	271.6	617.2	39	3.03	2.8×10	66	0.35	128	32	0.077
			0, -49	49	271.6	617.2	39	3.07		63	0.35	110	35	0.068
			0, -100	49	271.6	617.1	39	3.11		72	0.30	88	30	0.065
			1, -149	48	271.6	617.1	39	3.16		72	0.29	89	30	0.089
			3, -199	48	271.6	616.9	39	3.21		51	0.46	131	45	0.065
			2, -249	47	271.6	616.9	39	3.26		86	0.22	89	21	0.067
2009 May 9	0	910, 668	0, 0	66	270.6	614.6	36	2.11	0.8×60	52	0.45	18	10	0.072
			1, -153	66	270.6	614.6	36	2.12		49	0.50	19	15	0.031
			3, -304	65	270.6	614.6	36	2.13		49	0.47	19	16	0.026
			-154, -2	65	270.5	614.6	36	2.14		51	0.48	25	17	0.036
			-153, -154	65	270.5	614.7	36	2.15		47	0.58	30	25	0.036
			-152, -305	64	270.5	614.7	36	2.16		50	0.47	27	22	0.038
			-305, -4	64	270.8	614.7	35	2.17		50	0.51	23	19	0.034
			-305, -155	64	271.0	614.7	35	2.18		56	0.38	26	12	0.041
			-302, -306	63	271.0	614.7	35	2.20		63	0.30	22	13	0.033

Table 1—Continued

Date[a] (UT)	PA (deg)	$(X,Y)_{GS}$[b] (pix)	$\Delta(X,Y)$[c] (pix)	El (deg)	Temp (K)	Pressure (mbar)	RH[d] %	ΔR[e] (mas)	$t_{exp,i} \times$coadd (sec)	$\langle$FWHM$\rangle$ (mas)	$\langle$Strehl$\rangle$	N stars detected	N stars used	$\langle\sigma_{pos}\rangle$[f] (pix)
2009 May 9	90	365, 411	0, 0	62	270.8	614.6	35	2.27	0.8×60	49	0.49	25	19	0.025
			2, -153	61	270.8	614.6	35	2.29		50	0.48	24	17	0.028
			0, -302	61	270.8	614.5	35	2.31		50	0.47	10	8	0.031
			-151, -1	60	270.8	614.5	35	2.33		50	0.48	28	19	0.061
			-152, -154	60	270.8	614.5	36	2.35		47	0.56	29	22	0.035
			-149, -304	59	270.8	614.5	36	2.37		46	0.67	26	20	0.020
			-302, -4	59	270.6	614.5	36	2.40		46	0.61	35	24	0.023
			-304, -156	58	270.7	614.5	34	2.42		46	0.64	29	26	0.025
			-301, -305	58	270.7	614.5	34	2.45		48	0.53	18	15	0.030
2009 May 9	315	697, 499	0, 0	56	271.1	614.5	33	2.55	0.8×60	45	0.67	38	27	0.055
			2, -152	55	271.1	614.5	33	2.58		45	0.68	48	29	0.055
			0, -304	55	271.0	614.4	34	2.62		45	0.67	58	30	0.060
			-152, 0	54	270.7	614.3	35	2.66		47	0.56	35	22	0.044
			-148, -154	54	270.7	614.3	35	2.69		56	0.32	21	13	0.085
			-149, -305	53	270.7	614.3	35	2.74		50	0.45	43	18	0.078
			-300, -2	53	270.6	614.4	35	2.78		50	0.45	25	18	0.044
			-301, -154	52	270.6	614.5	35	2.82		59	0.29	21	13	0.063

[a]2008 June 3 data set taken in LGS-AO mode. All other data sets taken with NGS-AO.

[b]Position of guide star in first image of a given epoch.

[c]Positional offset of guide star in NIRC2 pixels relative to first pointing of epoch.

[d]Relative Humidity.

[e]Model of differential atmospheric refraction relative to center of image.

[f]Images thrown out are given a value of -1.0 for the average positional uncertainty (see text for details).

Table 2. Summary of GC Maser Mosaic Images

Date (UT)	PA (deg)	Start Pos[a] (pix)	$t_{exp,i}$×coadd (sec)	N_{exp}[b]	FWHM (mas)	Strehl
2005 June 30	0	851, 426	0.181×60	2	62	0.25
2006 May 3	0	852, 426	0.181×60	3	60	0.21
2007 Aug 12	0	852, 425	0.181×60	3	58	0.23
2008 May 15	0	856, 427	0.181×60	3	52	0.31
2009 June 28	0	855, 426	0.181×60	3	63	0.20

[a]X,Y position of IRS16C in first image of a given epoch

[b]Number of exposures per dither position

Table 3. Summary of New Keck Central 10" Imaging Observations

Date (UT)	Frames obtained	Frames used	Co-add $\times T_{exp}$ (s)	FWHM (mas)	Strehl	Number[a] of Stars	K_{lim} (mag)	Positional Error[b] (mas)
2008 May 15	138	134	10×2.8	54	0.25	2089	19.0	0.08
2008 Jul 24	179	104	10×2.8	58	0.27	2189	19.0	0.06
2009 May 1-4	311	149	10×2.8	57	0.29	2444	19.0	0.10
2009 Jul 24	146	75	10×2.8	62	0.21	1701	19.0	0.13
2009 Sep 9	55	43	10×2.8	61	0.27	2495	19.0	0.29

[a]The number of stars detected within 4" of Sgr A*.

[b]The median positional uncertainties are estimated using stars brighter than K<15 within $4''$ from Sgr A*.

Table 4. Summary of New Keck Spectroscopic Observations

Date (UT)	Filter: Spectral Range (μm)	Pixel Scale (mas)	No. Exp $\times T_{exp}$ (s)	S/N[a]	Calibration Stars (G2/A0)
2008 May 16	Kn3: 2.121 - 2.229	35	11×900	67	HD 193193/HD 195500
2008 Jul 25	Kn3: 2.121 - 2.229	35	9×900	57	HD 193193/HD 195500
2009 May 6	Kn3: 2.121 - 2.229	35	12×900	55	HD 193193/HD 195500

[a]The SNR is per spectral pixel and is calculated between 2.13 and 2.145 μm. The width of a spectral pixel is roughly 2.5 .

Table 5. Measurements of SiO Masers

Star Name	[IR − Radio] Position			Uncertainty in Radio		Uncertainty in IR Centroid		Error in Alignment		Distortion Error [a]		σ Offset		ΔR [b]
	X (mas)	Y (mas)	Total (mas)	X (mas)	Y (mas)	X (mas)	Y (mas)	X (mas)	Y (mas)	X (mas)	Y (mas)	X	Y	(mas)
IRS 9 (Avg)	1.92	0.80	2.13	0.52	1.08	0.85	0.99	0.66	0.66	1.53	1.53	0.92	0.33	-2.27
2005 June	1.70	1.00	1.97	0.40	0.80	0.25	0.44	0.50	0.70	1.52	1.53	1.02	0.52	-2.95
2006 May	3.10	1.90	3.64	0.40	0.90	2.41	2.46	0.50	0.40	1.54	1.53	1.06	0.62	-2.01
2007 August	1.40	0.80	1.61	0.50	1.10	0.48	0.84	0.50	0.30	1.53	1.53	0.80	0.38	-1.77
2008 May	2.10	0.30	2.12	0.60	1.20	0.40	0.51	0.80	1.10	1.53	1.53	1.12	0.13	-1.79
2009 June	1.30	0.00	1.30	0.70	1.40	0.70	0.73	1.00	0.80	1.53	1.53	0.63	0.00	-2.84
IRS 7 (Avg)	2.44	7.80	8.19	5.28	5.30	0.27	0.28	0.38	1.04	1.55	1.54	0.44	1.38	2.24
2005 June	2.60	5.80	6.36	5.00	5.00	0.14	0.48	0.40	0.80	1.56	1.54	0.49	1.09	2.21
2006 May	2.10	7.90	8.17	5.10	5.10	0.40	0.26	0.20	0.50	1.55	1.54	0.39	1.47	2.25
2007 August	2.60	7.50	7.94	5.30	5.30	0.29	0.15	0.30	1.00	1.56	1.55	0.47	1.34	2.29
2008 May	2.10	9.10	9.34	5.40	5.40	0.23	0.22	0.40	1.40	1.56	1.55	0.37	1.57	2.30
2009 June	2.80	8.70	9.14	5.60	5.70	0.29	0.31	0.60	1.50	1.56	1.54	0.48	1.43	2.17
IRS 12N (Avg)	2.58	3.26	4.41	1.00	1.60	2.78	3.78	0.98	0.92	1.51	1.51	0.78	0.83	-2.98
2005 June	1.80	5.40	5.69	0.80	1.30	0.51	0.90	0.70	0.90	1.52	1.52	0.94	2.28	-2.53
2006 May	4.00	1.30	4.21	0.90	1.40	3.09	1.51	0.30	0.60	1.51	1.51	1.12	0.50	-3.13
2007 August	0.80	0.40	0.89	1.00	1.60	0.24	2.06	0.90	0.60	1.51	1.52	0.39	0.13	-3.35
2008 May	3.00	5.60	6.35	1.10	1.80	1.48	5.93	1.40	1.30	1.51	1.51	1.08	0.86	-3.36
2009 June	3.30	3.60	4.88	1.20	1.90	8.59	8.53	1.60	1.20	1.50	1.49	0.37	0.40	-2.54
IRS 28 (Avg)	3.42	3.80	5.29	1.50	1.48	1.30	2.13	0.72	0.62	1.54	1.52	1.28	1.34	-1.81
2005 June	4.50	5.50	7.11	1.10	1.00	1.54	0.42	0.70	0.70	1.54	1.53	1.77	2.75	-3.09
2006 May	1.70	3.00	3.45	1.20	1.10	1.48	5.16	0.60	0.40	1.53	1.52	0.68	0.54	-1.33
2007 August	2.60	0.30	2.62	1.50	1.50	2.03	1.45	0.50	0.30	1.54	1.52	0.87	0.12	-0.84
2008 May	4.20	6.70	7.91	1.70	1.70	0.96	1.71	0.90	1.00	1.54	1.52	1.59	2.22	-0.87
2009 June	4.10	3.50	5.39	2.00	2.10	0.50	1.91	0.90	0.70	1.53	1.51	1.51	1.06	-2.93
IRS 10EE (Avg)	0.66	2.24	2.35	0.58	0.58	0.35	0.32	0.48	0.66	1.57	1.52	0.37	1.25	2.11
2005 June	0.40	1.40	1.46	0.50	0.50	0.09	0.63	0.60	0.50	1.57	1.52	0.23	0.78	1.12
2006 May	0.90	3.10	3.23	0.50	0.50	0.80	0.25	0.40	0.30	1.57	1.52	0.48	1.88	2.46
2007 August	1.10	2.50	2.73	0.60	0.60	0.35	0.26	0.30	0.70	1.57	1.52	0.63	1.39	2.89

Table 5—Continued

Star Name	[IR – Radio] Position			Uncertainty in Radio		Uncertainty in IR Centroid		Error in Alignment		Distortion Error [a]		σ Offset		ΔR [b]
	X (mas)	Y (mas)	Total (mas)	X (mas)	Y (mas)	X (mas)	Y (mas)	X (mas)	Y (mas)	X (mas)	Y (mas)	X	Y	(mas)
2008 May	0.10	1.70	1.70	0.60	0.60	0.25	0.12	0.60	0.90	1.57	1.52	0.06	0.91	2.88
2009 June	0.80	2.50	2.62	0.70	0.70	0.27	0.36	0.50	0.90	1.57	1.52	0.44	1.29	1.20
IRS 15NE (Avg)	1.00	3.36	3.64	0.66	1.10	0.27	0.42	0.38	1.32	1.57	1.57	0.57	1.37	4.64
2005 June	2.30	2.90	3.70	0.50	0.90	0.29	0.24	0.50	1.00	1.58	1.57	1.31	1.39	4.42
2006 May	1.50	1.90	2.42	0.60	1.00	0.10	0.49	0.40	0.60	1.58	1.57	0.86	0.94	4.70
2007 August	0.30	3.30	3.31	0.70	1.10	0.40	0.60	0.20	1.30	1.57	1.57	0.17	1.38	4.85
2008 May	0.30	4.40	4.41	0.70	1.20	0.08	0.19	0.40	1.80	1.57	1.57	0.17	1.64	4.86
2009 June	0.60	4.30	4.34	0.80	1.30	0.50	0.59	0.40	1.90	1.57	1.58	0.32	1.51	4.37
IRS 17 (Avg)	2.72	0.84	2.96	3.48	4.04	0.39	0.28	0.86	0.62	1.58	1.52	0.68	0.25	2.95
2005 June	1.90	1.00	2.15	1.60	2.00	0.28	0.03	0.90	0.50	1.58	1.52	0.78	0.39	1.27
2006 May	2.00	1.60	2.56	2.30	2.80	0.83	0.38	0.60	0.50	1.58	1.53	0.67	0.49	3.55
2007 August	2.00	1.30	2.39	3.60	4.10	0.57	0.48	0.60	0.70	1.58	1.52	0.50	0.29	4.28
2008 May	4.10	0.20	4.10	4.40	5.00	0.15	0.23	1.20	0.70	1.58	1.53	0.85	0.04	4.26
2009 June	3.60	0.10	3.60	5.50	6.30	0.13	0.31	1.00	0.70	1.59	1.52	0.62	0.02	1.41

[a]Distortion error includes the residual distortion term described in the text.

[b]Differential Atmospheric Refraction relative to the center of the image

Table 6. NIRC2 Plate Scale and Orientation

Method	Plate Scale (mas/pix)	Orientation (deg)
Calibrated w.r.t. ACS observations of M92[a]	$9.949 \pm 0.002 \pm 0.001$	$0.252 \pm 0.011 \pm 0.002$
2007 June	$9.948 \pm 0.001 \pm 0.001$	$0.249 \pm 0.006 \pm 0.002$
2007 July	$9.948 \pm 0.001 \pm 0.001$	$0.256 \pm 0.006 \pm 0.002$
2008 April	$9.946 \pm 0.007 \pm 0.001$	$0.276 \pm 0.030 \pm 0.002$
2008 June	$9.952 \pm 0.003 \pm 0.001$	$0.270 \pm 0.009 \pm 0.002$
2008 July	$9.951 \pm 0.002 \pm 0.001$	$0.248 \pm 0.004 \pm 0.002$
2009 May	$9.949 \pm 0.002 \pm 0.001$	$0.282 \pm 0.013 \pm 0.002$
Calibrated w.r.t. VLA observations of GC Masers[a]	9.953 ± 0.002	0.252 ± 0.012
2005 June	9.953 ± 0.001	0.238 ± 0.002
2006 May	9.955 ± 0.001	0.251 ± 0.002
2007 August	9.950 ± 0.001	0.258 ± 0.002
2008 May	9.954 ± 0.001	0.275 ± 0.004
2009 June	9.952 ± 0.001	0.260 ± 0.004
Final Value[a]	9.952 ± 0.003	0.252 ± 0.013

Note. — Statistical (first) and absolute (second) uncertainties are shown for the ACS observations (see §4.1).

[a]Weighted averages are taken for the final values for each method and for the overall final value. We use the more conservative RMS errors as the uncertainties on these values.

Table 7. Absolute Astrometry of SiO Masers

Maser	T_0 (year)	X_0[a] (arcsec)	Y_0[a] (arcsec)	V_x (mas/yr)	V_y (mas/yr)
IRS 9	2007.5	5.676	-6.331	3.16 ± 0.60	1.83 ± 0.59
IRS 7	2007.2	0.034	5.522	-0.53 ± 0.52	-4.19 ± 0.62
IRS 12N	2006.6	-3.265	-6.912	-0.92 ± 1.07	-1.51 ± 1.08
IRS 28	2007.6	10.480	-5.829	2.00 ± 0.70	-5.55 ± 0.68
IRS 10EE	2007.4	7.684	4.199	-0.11 ± 0.53	-2.01 ± 0.55
IRS 15NE	2007.1	1.211	11.274	-2.66 ± 0.53	-5.15 ± 0.68
IRS 17	2007.5	13.142	5.561	-1.10 ± 0.58	-1.07 ± 0.54

[a]Uncertainties in the positions of the masers are taken as the average intercept error described in §4.1, which are 1.6 mas and 2.1 mas for X and Y, respectively.

Table 8. Updated NIRC Reimager Distortion Coefficients

i	$X(a_i)$	$Y(b_i)$
0	1.6178×10^{-3}	1.9058×10^{-3}
1	9.9723×10^{-1}	-1.1409×10^{-3}
2	-2.3980×10^{-3}	1.0035

Table 9. Summary of Keck Astrometric and Photometric Measurements for S0-2

UT Date	K_{obs} (mag)	X (mas)[a]	Y (mas)[a]
1995.439	14.20 ± 0.12	-44.84 ± 1.84	171.49 ± 1.02
1996.485	14.16 ± 0.28	-57.56 ± 6.88	165.92 ± 6.92
1997.367	14.15 ± 0.27	-61.09 ± 1.93	144.46 ± 1.93
1999.333	14.02 ± 0.08	-64.86 ± 1.86	97.94 ± 1.86
1999.559	14.09 ± 0.04	-67.39 ± 1.44	93.64 ± 1.32
2000.305	13.97 ± 0.16	-61.57 ± 3.77	70.48 ± 3.03
2000.381	14.14 ± 0.06	-64.98 ± 1.18	67.66 ± 1.14
2000.548	14.10 ± 0.26	-63.49 ± 1.24	62.88 ± 1.24
2000.797	14.05 ± 0.31	-61.19 ± 5.61	50.76 ± 5.26
2001.351	14.18 ± 0.27	-54.13 ± 1.80	29.60 ± 1.83
2001.572	14.15 ± 0.26	-50.88 ± 1.56	18.09 ± 1.55
2003.303	14.26 ± 0.25	38.86 ± 2.04	72.80 ± 1.89
2003.554	14.27 ± 0.24	39.09 ± 1.03	84.21 ± 0.98
2003.682	14.33 ± 0.24	35.02 ± 2.03	89.39 ± 2.01
2004.327	14.20 ± 0.07	34.92 ± 0.98	116.58 ± 0.94
2004.564	14.20 ± 0.06	32.13 ± 1.37	123.03 ± 1.39
2004.567	14.28 ± 0.26	33.78 ± 1.19	125.78 ± 1.18
2004.660	14.20 ± 0.08	29.76 ± 1.41	127.01 ± 1.42
2005.312	14.15 ± 0.08	22.55 ± 1.16	144.23 ± 1.16
2005.495	14.27 ± 0.11	23.01 ± 2.09	147.45 ± 2.08
2005.566	14.16 ± 0.15	20.30 ± 1.73	150.43 ± 1.77
2005.580	14.19 ± 0.12	23.27 ± 1.14	148.64 ± 1.13
2006.336	14.21 ± 0.17	11.97 ± 0.15	161.86 ± 0.13
2007.612	14.06 ± 0.16	0.35 ± 1.22	173.89 ± 1.22
2008.371	14.11 ± 0.16	-11.34 ± 0.12	179.46 ± 0.12
2008.562	14.09 ± 0.19	-13.31 ± 0.16	180.03 ± 0.17
2009.340	14.15 ± 0.18	-22.47 ± 0.10	180.24 ± 0.11
2009.561	14.14 ± 0.19	-24.69 ± 0.17	180.17 ± 0.20
2009.689	14.13 ± 0.22	-26.01 ± 0.19	179.75 ± 0.20

[a]X and Y are the relative positions in the east-west and north-sorth direction, with increasing values to the east and north, respectively. These values are in our absolute coordinate system (i.e., relative to Sgr A*-radio; see §4.1), but the uncertainties do not include the uncertainties in the absolute coordinate system. Measurements that are confused with other known sources are not included in this table.

Table 10. Summary of New Keck Radial Velocity Measurements for S0-2

	Radial Velocity (km s^{-1})	
UT Date	Observed	LSR
2008 May 16	-443 ± 32	-417 ± 32
2008 Jul 25	-373 ± 43	-380 ± 43
2009 May 6	-315 ± 32	-285 ± 32

Table 11. Orbital Elements for S0-2 and the Implied Black Hole Properties

Parameter	
Distance (R_0) (kpc)	8.0 ± 0.4
Period (P) (yr)	15.87 ± 0.13
Semimajor axis (a) (mas)	126.9 ± 2.8
Eccentricity (e)	0.8920 ± 0.0044
Time of closest approach (T_0) (yr)	2002.346 ± 0.008
Inclination (I) (inc)	135.24 ± 1.07
Position angle of the ascending node (Ω) (deg)	226.92 ± 0.74
Angle to periapse (ω) (deg)	66.5 ± 1.0
X dynamical center ($X_0 - X_{SgrA^*-radio}$) (mas)	3. ± 0.958
Y dynamical center ($Y_0 - Y_{SgrA^*-radio}$) (mas)	-2 ± 1.393
X velocity (V_x) (mas yr^{-1})	0.13 ± 0.10
Y velocity (V_y) (mas yr^{-1})	-0.05 ± 0.12
Z velocity (V_z) (km s^{-1})	-21 ± 20
Mass (M_{BH}) ($10^6 M_\odot$	4.14 ± 0.47
Density (ρ) ($10^{15} M_\odot$ pc^{-3})	6.3 ± 0.7
Periapse distance (R_{min}) (mpc)	0.551 ± 0.039

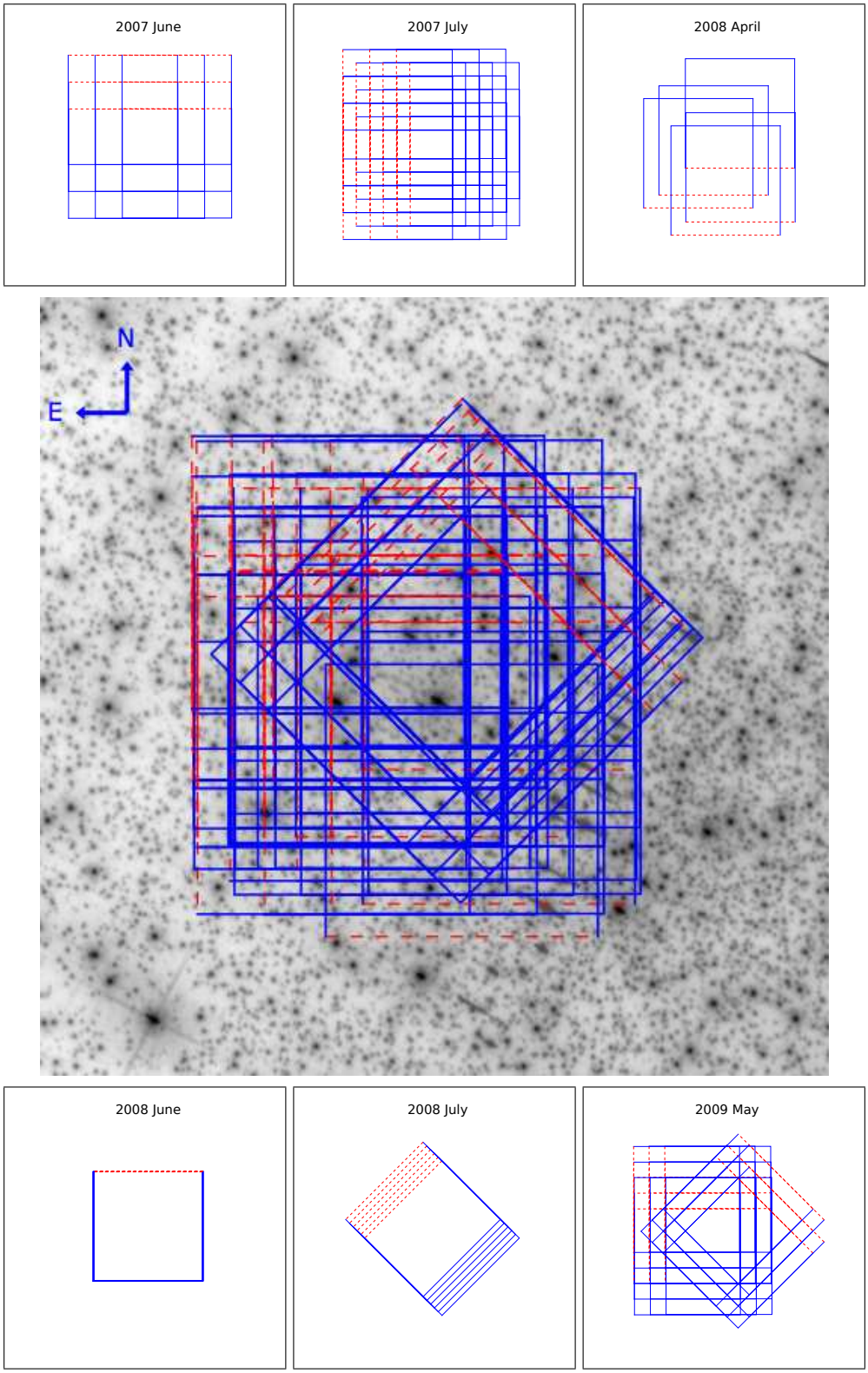

Fig. 1.— ACS/WFC image with the 79 NIRC2 pointings. The red dashed side of each NIRC2 box denotes the top of the detector's field of view. Each NIRC2 field is 10×10", while the ACS image shown is ∼30×30". The pattern for the individual epochs' exposures are shown in the insets.

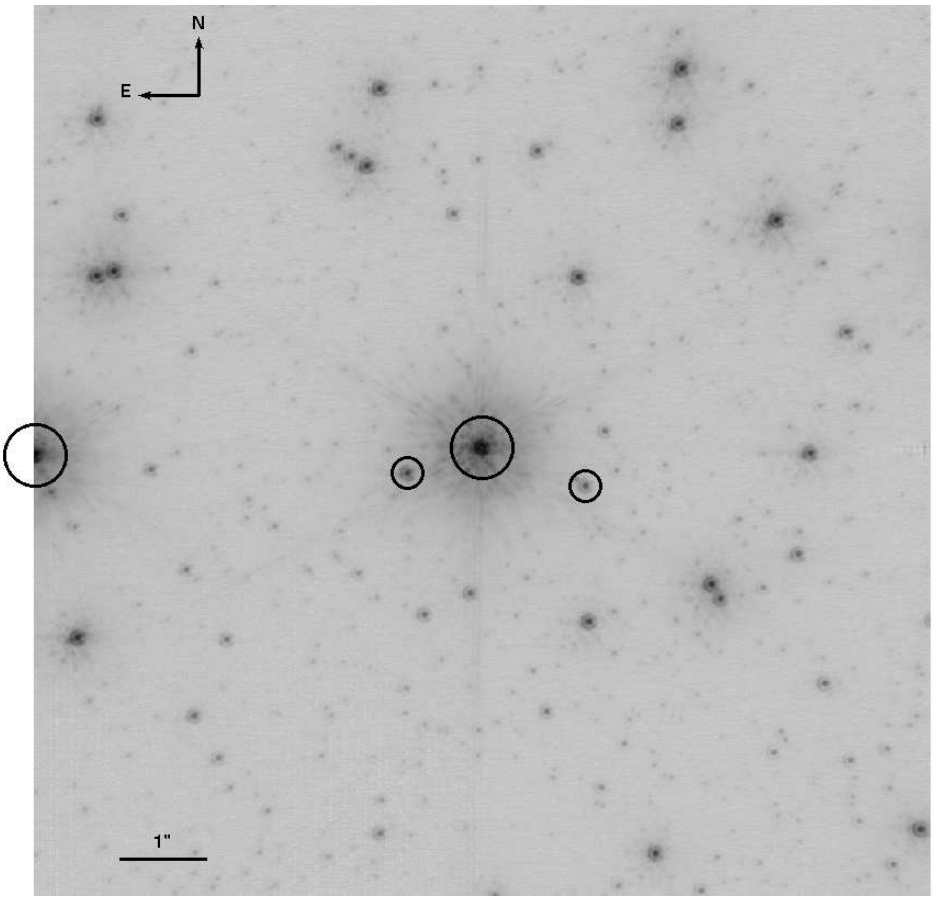

Fig. 2.— Diffraction-limited NGSAO NIRC2 image of one of the M92 fields used to characterize the optical distortion in the NIRC2 camera. The circled stars at the center of the image, the NGS and two fainter stars, are present in most of the M92 NIRC2 observations and are used to register the images, each of which had a different position/orientation on the sky. The NGS and the circled star ∼5" to its east were almost always detected at levels that saturated the detector and were therefore removed from the analysis (see text).

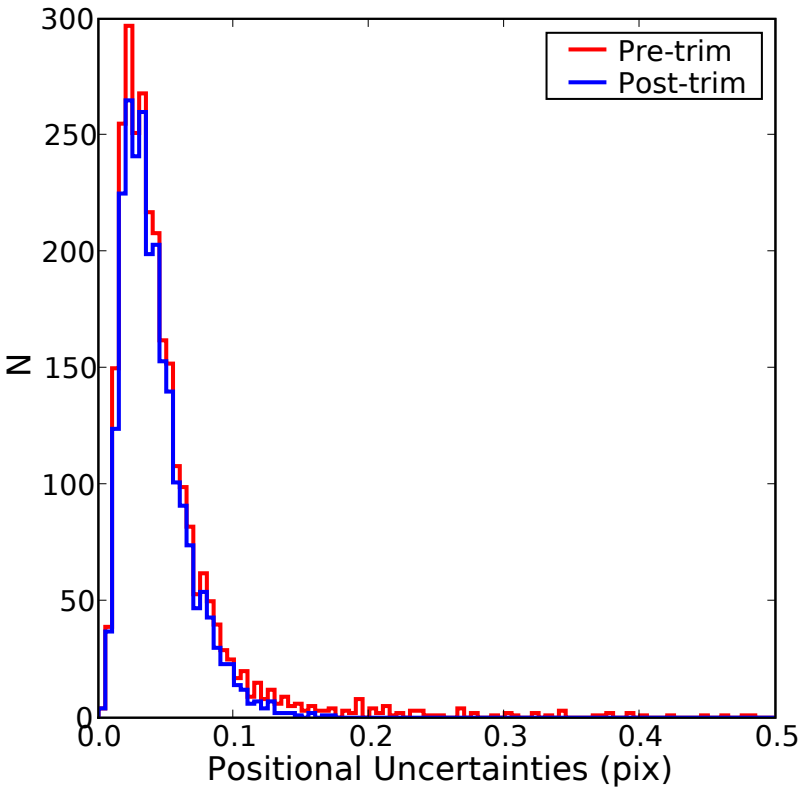

Fig. 3.— NIRC2 (plate scale ∼10 mas/pix) positional uncertainties for stars matched to the ACS/WFC star list before (*red*) and after (*blue*) removing all outliers (see text). RMS uncertainties are calculated from the three images taken at each position on the sky.

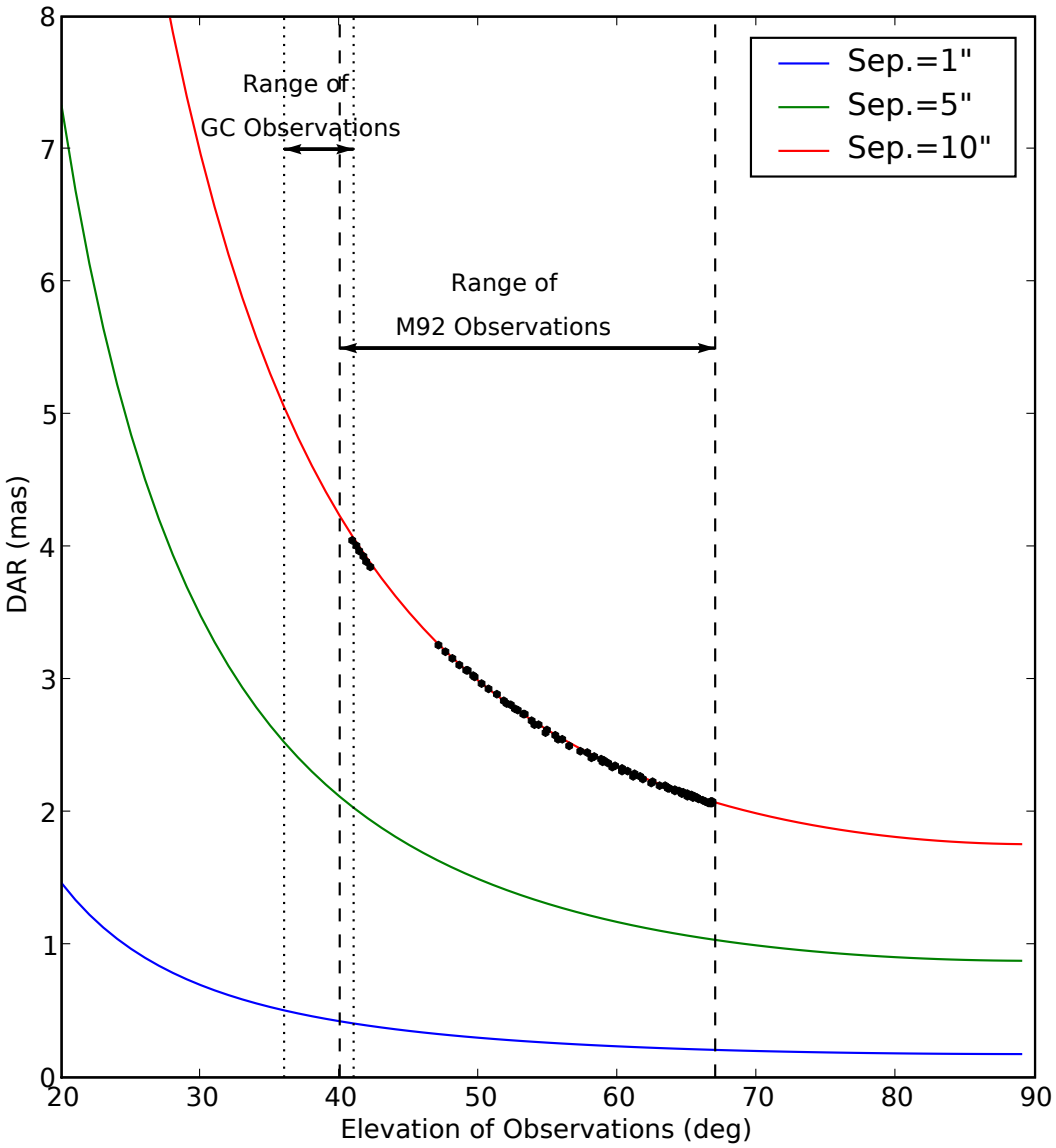

Fig. 4.— The predicted differential atmospheric refraction at a range of elevation angles for *typical* observing conditions at Keck. DAR causes the separation of two stars to appear smaller along the zenith direction and the change in the separation is shown for three pairs of stars separated by 1”, 5”, and 10”. The black dots show the amount of DAR over the 10” field for each of the M92 observations used in the distortion solution. These are slightly offset from the predicted curve (*red*) because the atmospheric conditions differed slightly from the reference conditions used to generate the curves. The range of our GC and M92 observations are also shown.

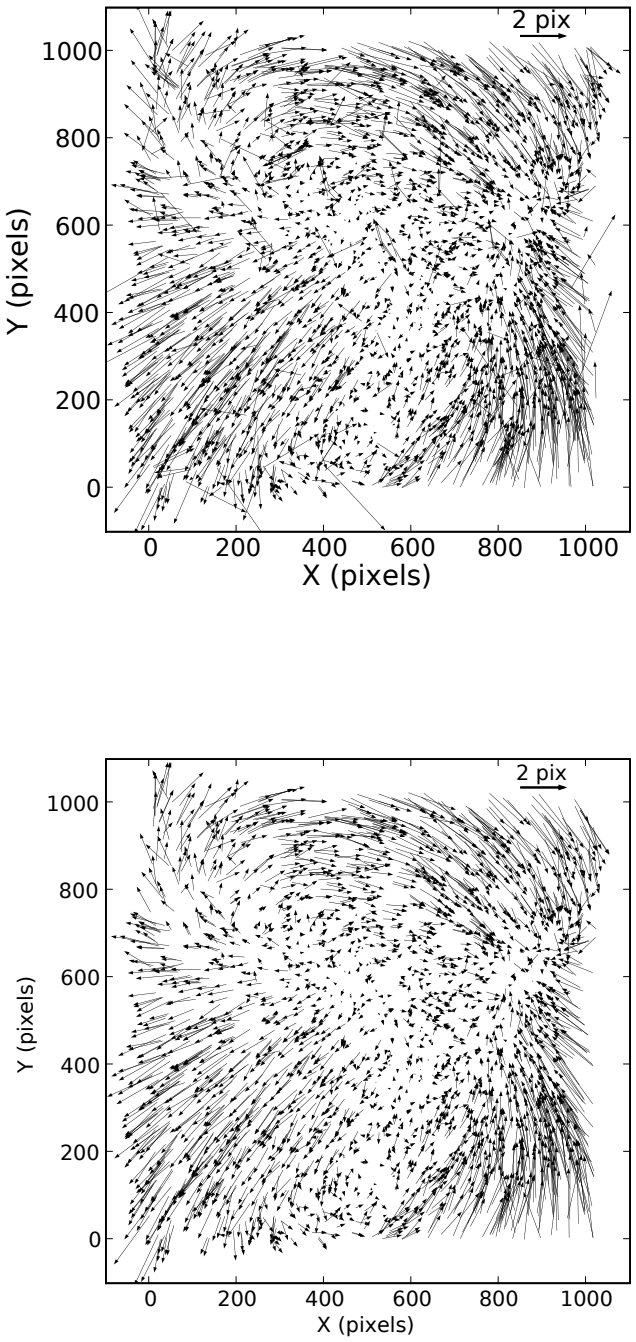

Fig. 5.— Optical distortion in the NIRC2 camera obtained from positional measurements of stars in the globular cluster M92. Arrows indicate the difference between measurements made with NIRC2 (*arrow tail*) and ACS/WFC (*arrow head*), which has a well characterized distortion solution to the ∼0.5 mas level (Anderson & King 2006; Anderson 2007). The two figures show pre- (*top*) and post- (*bottom*) trimming.

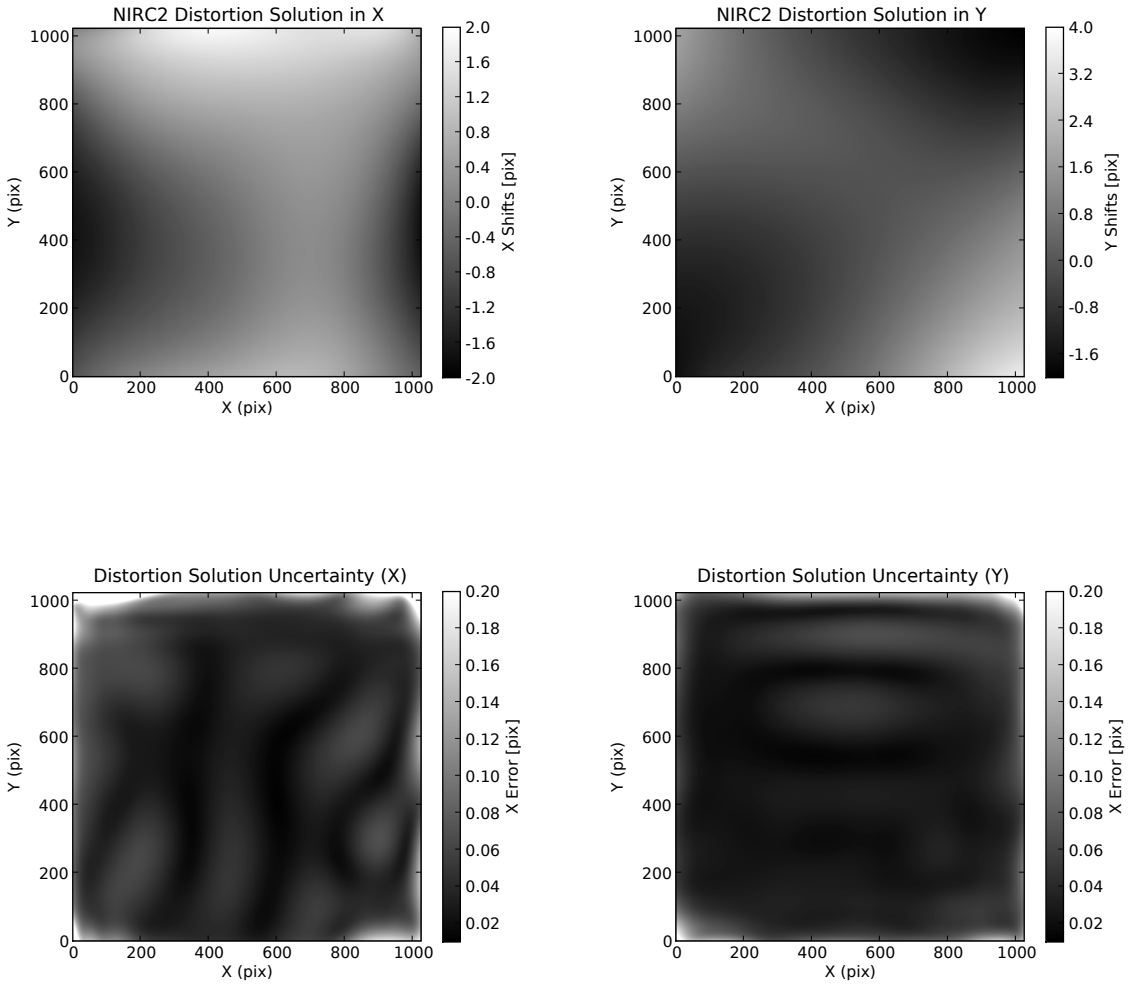

Fig. 6.— (*Top:*) Distortion solution in the form of a look-up table for X (*left*) and Y (*right*). The tables give the X and Y values for each pixel required to remove the optical distortion from NIRC2 images. This was generated by fitting a surface to the distortion map in the bottom of Figure 5. (*Bottom:*) RMS error of the 1000 simulations of the distortion solution in FITS file format for X (*left*) and Y (*right*). The images are shown in linear stretch.

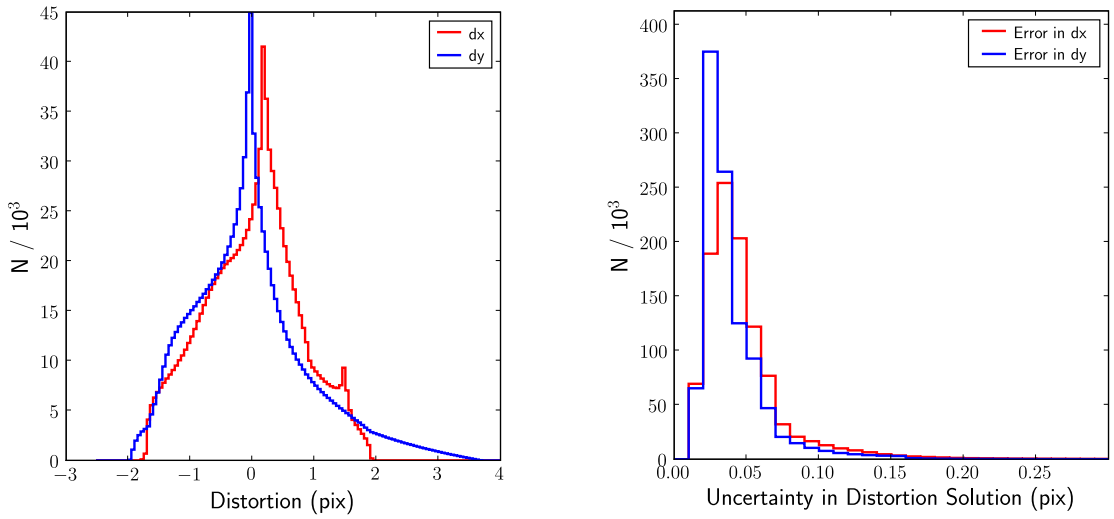

Fig. 7.— (*Left*) Distribution of the shifts in the distortion solution look-up table over all NIRC2 pixels. (*Right*) Distribution of the RMS uncertainties from the 1000 simulations of the distortion solution for X (*red*) and Y (*blue*). The average errors in X and Y are 0.05±0.04 and 0.04±0.02 pix, respectively.

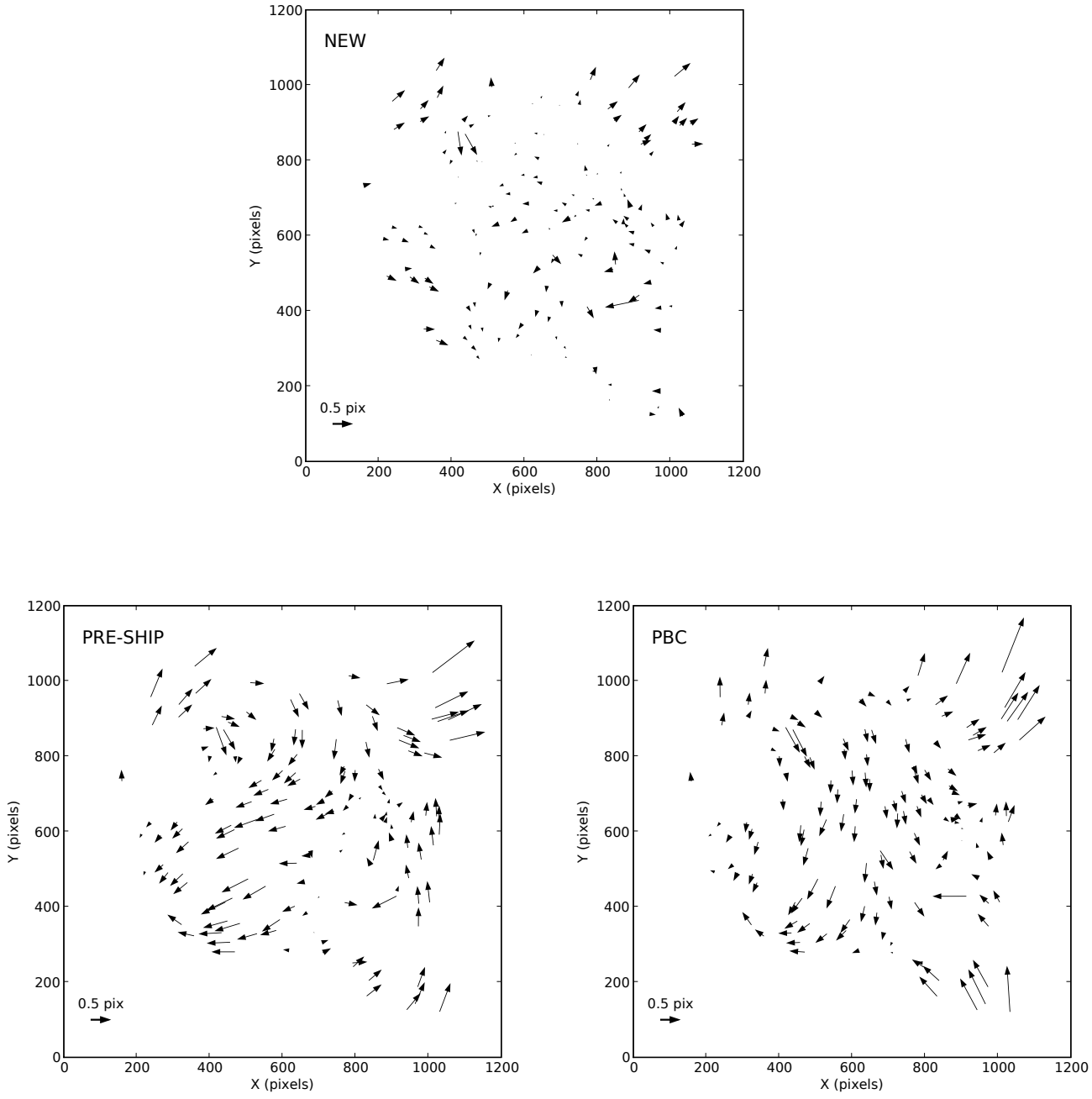

Fig. 8.— Differences between stellar positions in Galactic center images taken at PA=200 (*arrow tail*) and PA=0 (*arrow head*) after applying the pre-ship (*top left*), PBC (*top right*), and the new (*bottom*) distortion solution. While some residual distortion remains, much of the structure seen after using the pre-ship solution is removed with the new solution.

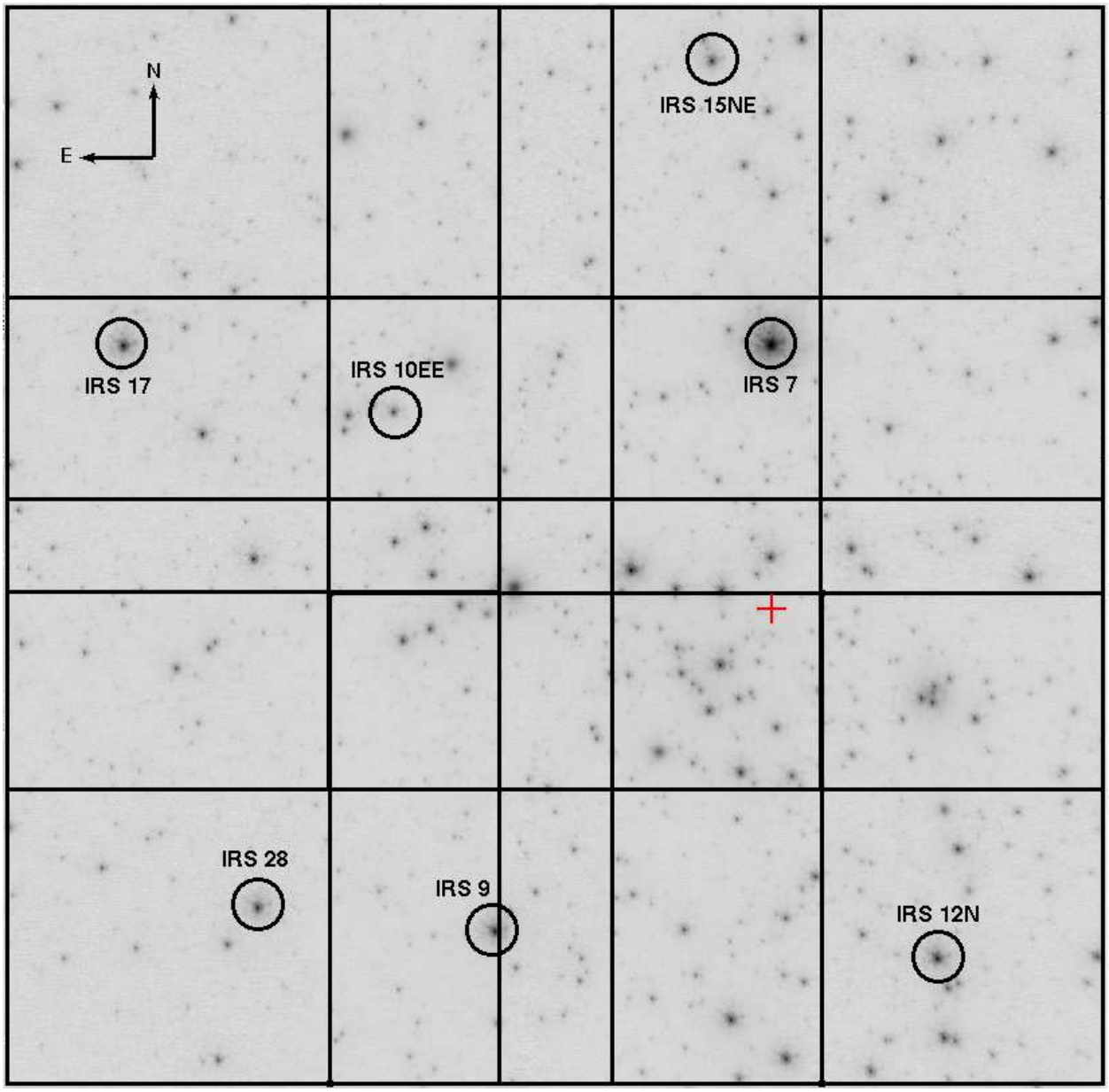

Fig. 9.— NIRC2 K' mosaic image of the Galactic center. The full field is 22"×22", approximately centered on Sgr A* (*red cross*). The black boxes show the nine dither positions making up the mosaic, with each box corresponding to the 10"×10" NIRC2 field of view. The 7 SiO masers used in our absolute astrometry are circled.

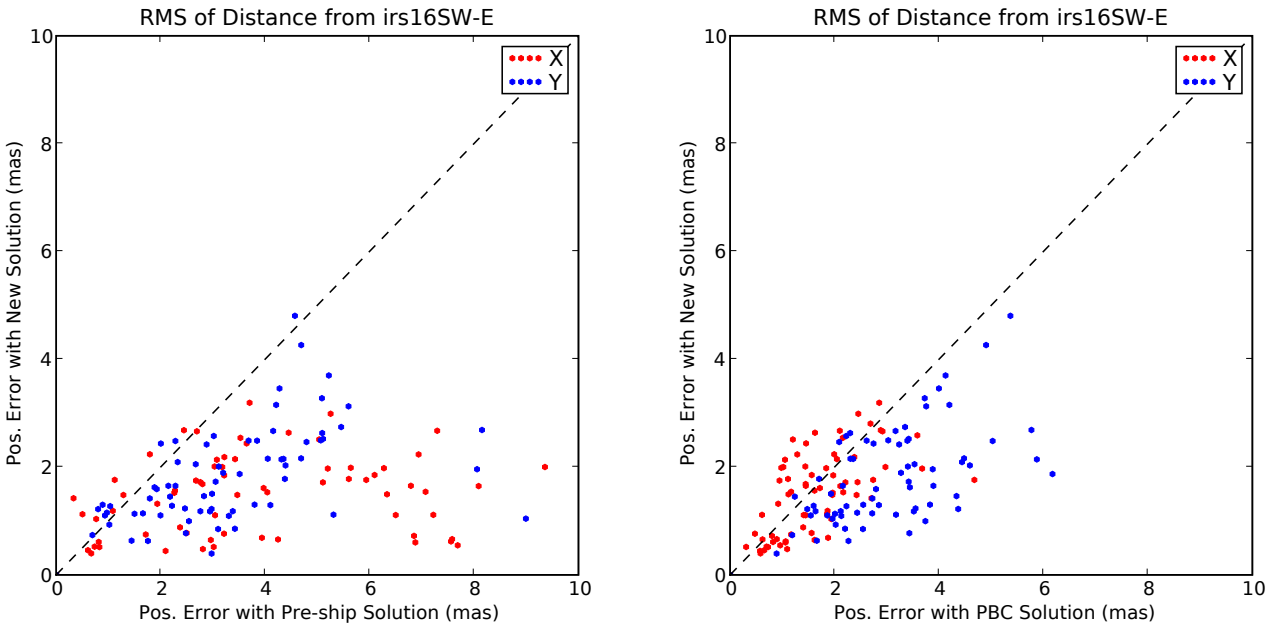

Fig. 10.— Pair-wise analysis on widely-dithered Galactic center data taken in 2006 May. The RMS of the positional offsets from IRS16SW-E are plotted. The plots compare the RMS values from images corrected with the new versus the pre-ship distortion solution (*left*) and the new versus the PBC distortion solution (*right*).

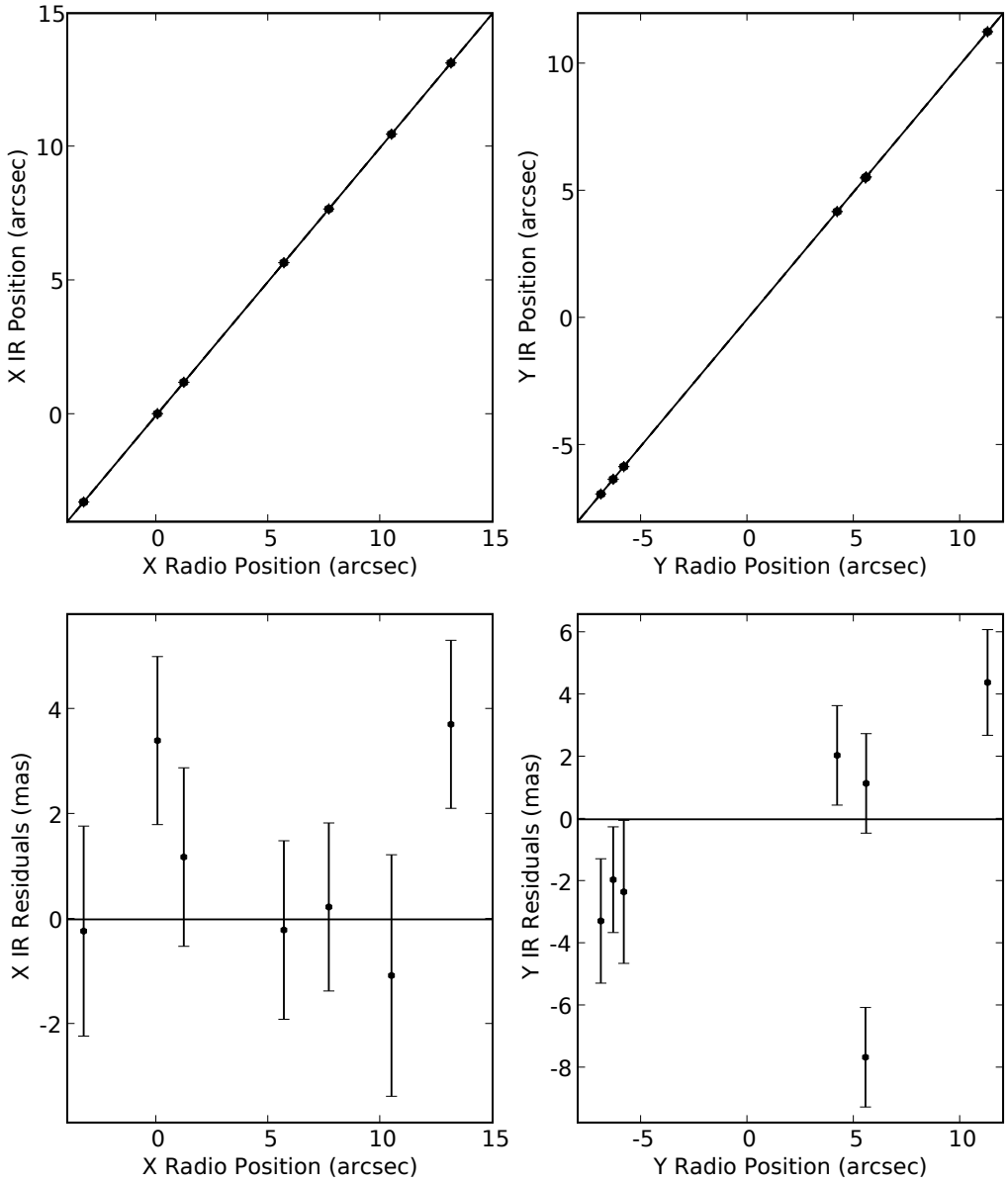

Fig. 11.— (*Top*) Absolute positions of Galactic center SiO masers in the infrared plotted against those in the radio for the 2007 August epoch, with the best fit line overplotted. Radio positions are propagated to this epoch using proper motions from Reid et al. (2007). Errors on both the data points and the best fit line are plotted. The best fit line for the 2007 August data give a slope and intercept of 0.99993 $\pm$ 0.00001 and -0.8 $\pm$ 1.0 mas for X, and 0.99978 $\pm$ 0.00001 and 1.4 $\pm$ 0.9 mas for Y, respectively. We use formal errors from the line fits. (*Bottom*) Residuals from the line fit for the IR positions (*in mas*) plotted against the radio position.

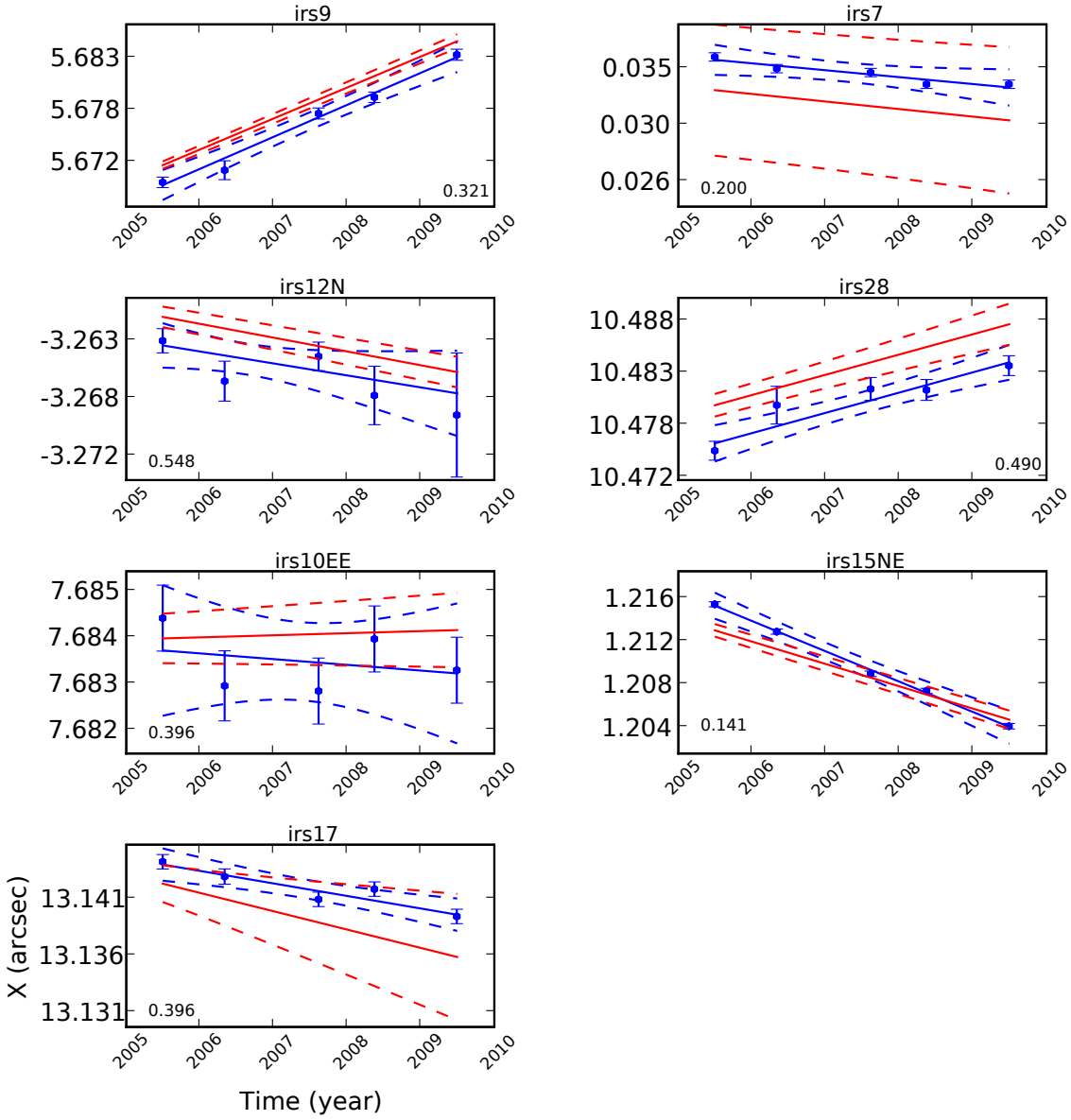

Fig. 12.— Absolute X positions of Galactic center SiO masers in the infrared as a function of time and the velocity model fit (*blue*) and the proper motion model for the radio (*red*). The 1σ errors on the line fits are shown as dashed lines. Radio proper motion measurements are taken from Reid et al. (2007). The positional uncertainties in the infrared have been rescaled such that the velocity χ^2_R=1 (see text).

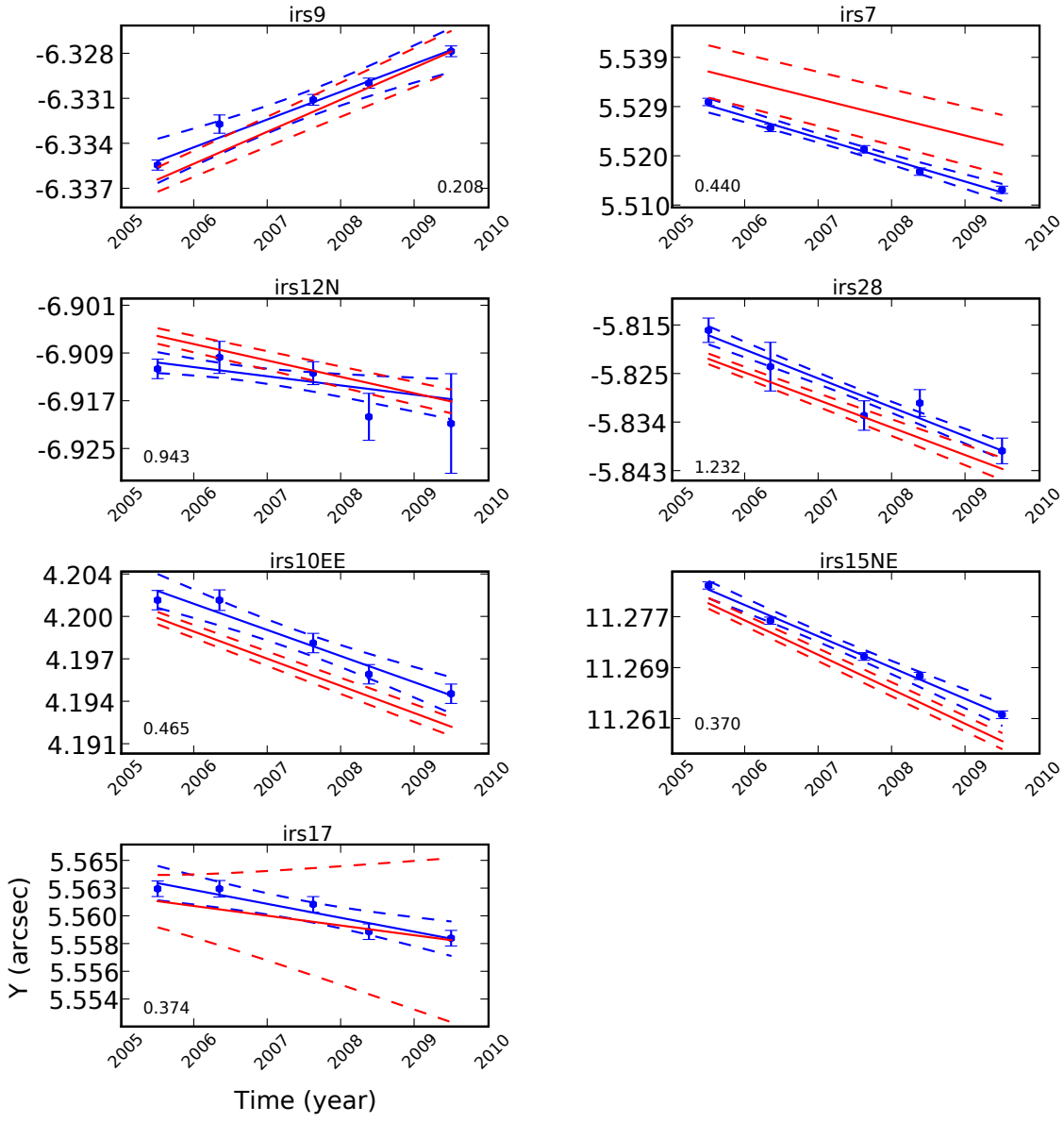

Fig. 13.— Same as Figure 12 but for Y positions.

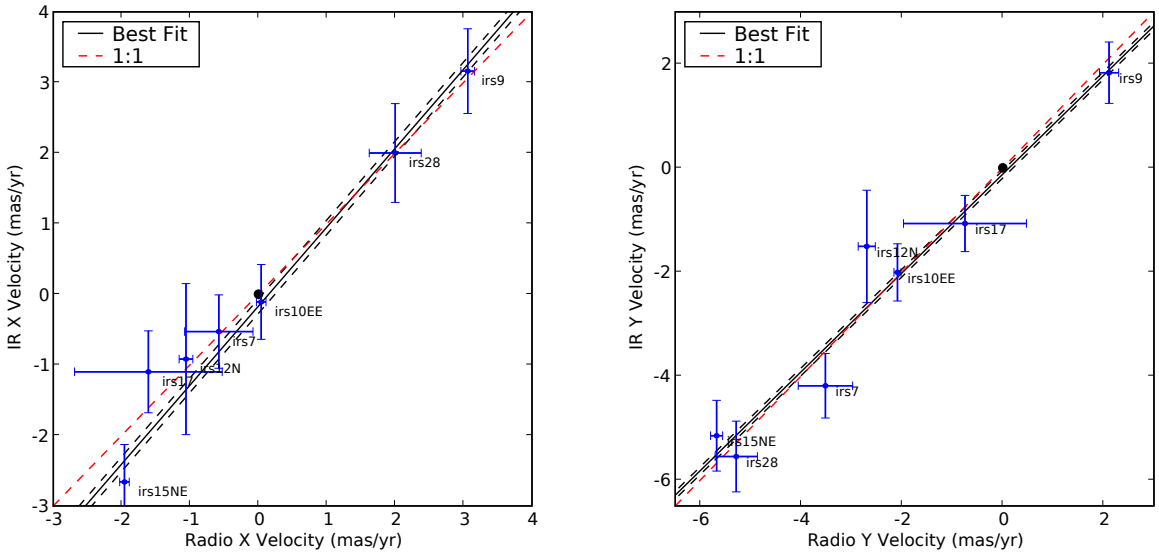

Fig. 14.— Proper motions of the SiO masers in the infrared plotted against those in the radio. X velocities are shown on the left, and Y velocities on the right. The solid black line shows a linear fit to the data, weighted by errors in both IR and radio proper motions, while the dashed black lines show the 1σ errors on the line fit. The dashed red line shows the 1:1 mapping.

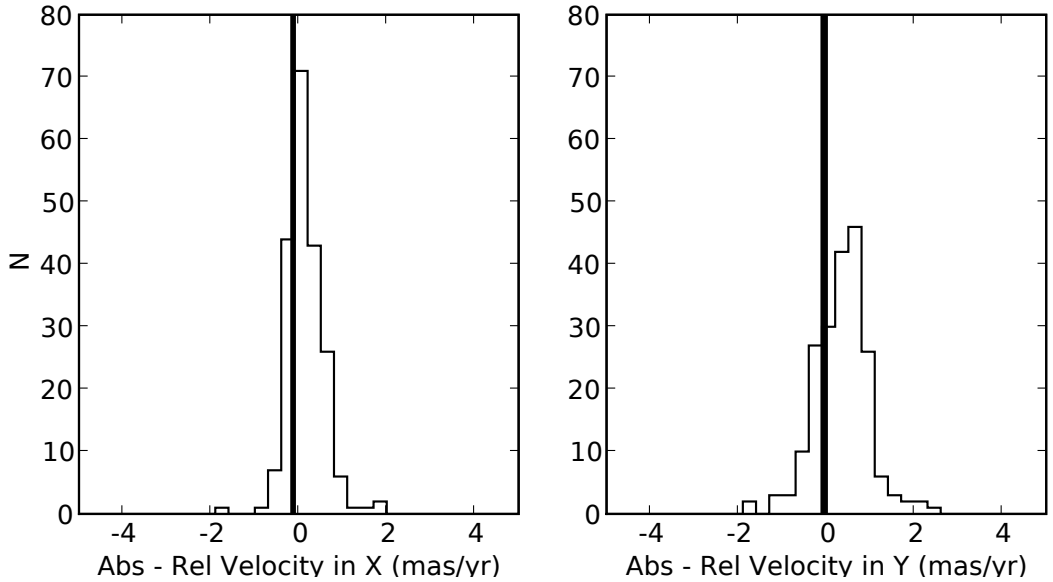

Fig. 15.— Histogram of the difference between absolute and relative velocities of the infrared stars in the Galactic center. The average velocity difference is 0.2 ± 0.4 and 0.3 ± 0.6 mas/yr in the East-West and North-South directions, respectively. The vertical bar shows the velocity of the black hole relative to the stellar cluster as derived from the orbit of S0-2 in this work.

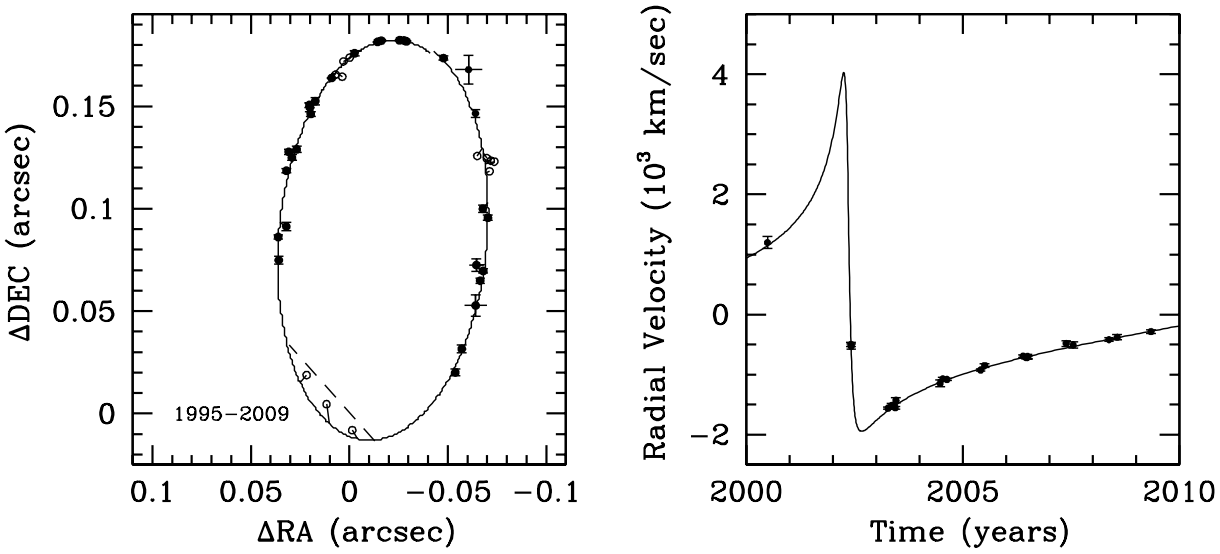

Fig. 16.— Best fit to the astrometric and radial velocity data for S0-2 assuming a Keplerian model in which the black hole's motion is left as a free parameter. Filled data points represent the points included in the fit, while unfilled data points (astrometry only) are those excluded due to source confusion. Uncertainties are shown for all filled data points. Errors for the unfilled points are not shown for clarity (these errors are comparable to the size of the points). The best fit model gives a reduced χ^2 of 1.174.

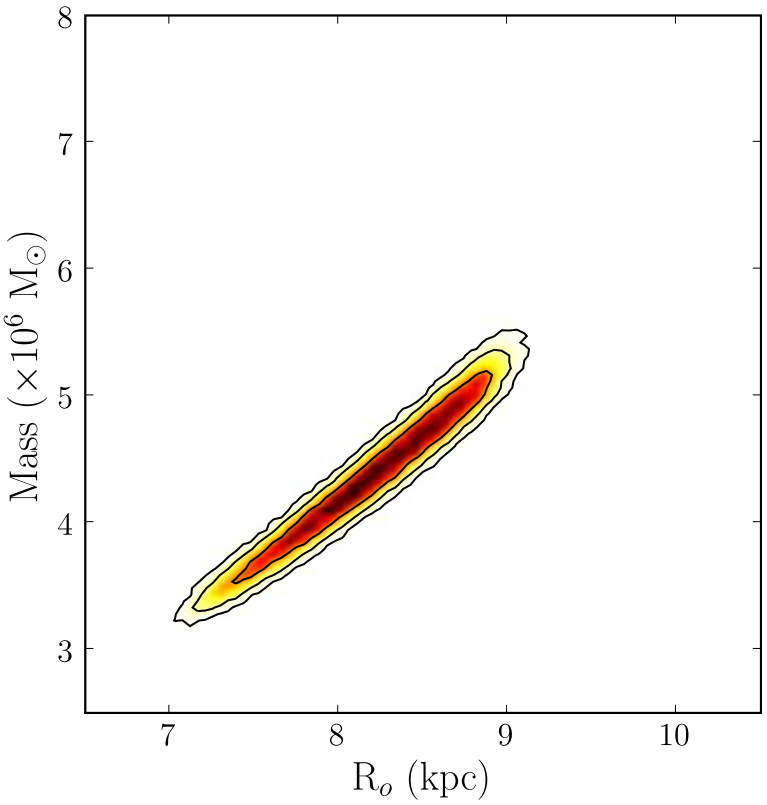

Fig. 17.— Density of solutions from the Monte Carlo simulations showing the correlation of the black hole's estimated mass and distance. Contours show the 68%, 95%, and 99.7% confidence limits.